Large-eddy simulation of an air-assisted liquid jet under a high-frequency transverse acoustic forcing

Nicolas Rutard, Luc-Henry Dorey, Clément Le Touze, S. Ducruix

Large-eddy simulation of an air-assisted liquid jet under a high-frequency transverse acoustic forcing

N. Rutard[1], L.-H. Dorey[1], C. Le Touze[1], and S. Ducruix[2]

[1]ONERA, DMPE, Université Paris-Saclay, F-92322 Châtillon, France
[2]Laboratoire EM2C, CNRS, CentraleSupélec, Université Paris-Saclay, 3 rue Joliot Curie, 91192 Gif-sur-Yvette cedex, France

November, 2019

Abstract

The present contribution falls in the scope of high-frequency combustion instabilities occurring in liquid rocket engines. Under subcritical operating conditions, numerical simulations have to render the effects of acoustic waves on the atomisation of liquid jets since these may impact the stability of the engine. Therefore, the present contribution aims at evaluating the ability of a particular numerical strategy adapted to the simulation of two-phase flows to render these interaction mechanisms. The selected strategy is based on the coupling between a diffuse interface method for the simulation of large liquid structures, and a kinetic-based Eulerian model for the description of droplets. The numerical simulation of an air-assisted liquid jet submitted to a transverse acoustic modulation is performed. The flattening of the liquid core under acoustic constraints is retrieved and induces an intensification of its stripping. In addition, thanks to appropriate coupling source terms, the modification of the spray shape as well as periodic oscillations of droplets are retrieved. The numerical strategy is thus proved to be adapted to deal with atomised liquid jets under transverse acoustic modulation and can be used for future numerical studies of high-frequency combustion instabilities.

Keywords: liquid rocket engine, subcritical operating condition, two-phase flow, air-assisted atomisation, acoustic modulation, large-eddy simulation

1 Introduction

The occurrence of High-Frequency (HF) combustion instabilities is a major issue in the design of Liquid Rocket Engines (LRE). In such high power density engines, the coupling between the injection system, the propellant jets, their combustion and the acoustic modes of the thrust chamber may induce a rapid growth of heat release rate fluctuations and cause dramatic damages to the propulsion system. Despite decades of substantial research mainly conducted via experiments (Harrje & Reardon 1972, Anderson & Yang 1995, Culick 2006), origins of this unstable phenomenon are still not fully understood, essentially due to 1) the complexity of coupling mechanisms involved, 2) the limited instrumentation access to the thrust chamber inherent in the severe operating conditions and 3) the significant cost of full-scale engine tests. As a result, to improve knowledge on this critical issue whilst meeting with present-day industrial's need to reduce engine design costs, a three-pronged approach emerged, combining experiments on lab-scale set-ups, high-performance Computational Fluid Dynamics (CFD) and low-order modelling (Poinsot 2017).

Last block of this triptych is used in industry for engine development stage and aims at predicting the stability of the propulsion system at low cost by modelling the unsteady heat release rate as a function of acoustic perturbations. For this purpose, both linear (*e.g.* Crocco & Zheng (1956)) and non-linear approaches (*e.g.* Culick (1976) or Noiray et al. (2008)) exist. Despite their fast, low cost and easy-to-use aspects, these low-order approaches require experimental or CFD analyses to set usually case-dependent modelling parameters.

To address this lack of generality, it is necessary to get a better insight on driving mechanisms of combustion instabilities for the entire scope of engine operating conditions. Two regimes can be identified for LOX injection, namely trans- and subcritical operating conditions. The former are related to high-thrust regimes during which pressure levels in the combustion chamber are higher than the critical pressure of oxygen (50 bar), which induces an injection of this propellant at a quasi gaseous-state. In this case, experiments have been performed on lab-scale configurations for non-reactive jets (Davis & Chehroudi 2007) in order to observe how coaxial flows respond to transverse acoustic perturbations. Similar experiments have been carried out later for reactive jets (see Hardi et al. (2014) for example) to understand how these acoustics/flow coupling mechanisms may in turn impact the flame behaviour. In addition, complementary investigations have been successfully carried out by means of CFD, either in gas/gas (Selle et al. 2014) or transcritical conditions (Hakim, Ruiz, Schmitt, Boileau, Staffelbach, Ducruix, Cuenot & Candel 2015, Hakim, Schmitt, Ducruix & Candel 2015, Gonzalez-Flesca et al. 2016, Urbano et al. 2016). All these contributions have led to a better understanding of coupling mechanisms between acoustic perturba-

tions and transcritical flames, which is essential to express general low-order models.

Subcritical conditions, on the other hand, correspond to low-thrust and transient operating phases and are characterised by pressure levels in the combustion chamber lower than the critical pressure of oxygen, resulting in a liquid-state injection of this propellant. Since physical mechanisms such as atomisation, fragmentation, droplet dispersion and vaporisation are sensitive to pressure and velocity fluctuations, the presence of a liquid phase may affect the flame response and participate to the thermoacoustic coupling (Oefelein & Yang 1993, Culick 2006). However, the level of understanding of these coupling mechanisms is somewhat lower than under transcritical conditions. That is why the present contribution focuses on subcritical conditions in particular. This issue has been investigated experimentally in the past by submitting round or coaxial liquid jets to acoustic modulation and different response mechanisms have been observed. First, it has been shown by Hoover et al. (1991), and confirmed later by Chehroudi & Talley (2002), that acoustics may flatten the central liquid core along the acoustic propagation axis. When dealing with coaxial jets, Baillot et al. (2009) explained this phenomenon by the suction effect induced by the heterogeneous distribution of acoustic radiation pressure around the liquid core. For acoustic pressure levels around 162 dB (peak-to-peak pressure amplitudes of 7% of the mean cavity pressure) and a modulation frequency around 1 kHz, the authors even demonstrated that this may lead to a drastic change in primary atomisation processes. The second effect of acoustics that has been noticed on the liquid core is the reduction of its length (Davis & Chehroudi 2007, Baillot et al. 2009). In the case of reactive two-phase flows submitted to peak-to-peak acoustic pressure amplitudes around 20% of the mean chamber pressure and frequencies between 1.8 kHz and 3.2 kHz, Méry et al. (2013) observed a direct impact of this phenomenon on the flame length, which may affect the stability of the system. The third effect of acoustics being noticed is the transverse oscillation of the liquid core at the acoustic modulation frequency. First observed for free liquid jets by Miesse (1955) and Buffum & Williams (1967) for minimum acoustic pressure levels of 140 dB (peak-to-peak acoustic pressure amplitudes of 0.6% of the mean cavity pressure) and a maximum modulation frequency of 500 Hz, this observation has been confirmed later for coaxial two-phase flows by Davis & Chehroudi (2007) with acoustic pressure levels of 180 dB (peak-to-peak acoustic pressure amplitudes of 4% of the mean cavity pressure) and a modulation frequency of 3 kHz. These oscillations have been interpreted as being caused by the periodic fluctuations of the gas phase velocity around the liquid jet. In the case of reactive two-phase flows, the same observations have been made for droplets (Méry et al. 2013), resulting in a periodic transverse movement of the flames that may drive HF combustion instabilities. Regarding the spray resulting from the atomisation process, another noticeable impact of acoustics has been observed by Baillot

et al. (2009) and consists in a transverse deviation of droplets due to acoustic radiation forces. In addition, Baillot et al. (2009) and Ficuciello et al. (2017) observed a drastic expansion of the spray angle in the direction orthogonal to the acoustic propagation axis. Given all these experimental observations, it appears that the combustion stability may thus be strongly affected by the impact of acoustics on the liquid phase. However, experiments alone are not sufficient to reach a complete understanding of all coupling mechanisms. As proved in transcritical conditions, CFD analyses of reactive and non-reactive jets under acoustic modulation are adapted to bring complementary observations. The numerical simulation of atomised liquid jets typical of LRE configurations is nevertheless challenging due to numerical difficulties arising from the disparity in time and length scales of various phenomena such as atomisation, fragmentation and vaporisation. On top of that, a significant lack of contribution is noticed in this domain.

Numerical simulations of stable cryogenic flames under subcritical conditions have been performed in the past by Jay et al. (2006) in a Reynolds-average Navier-Stokes approach, but such a method is not suitable for the simulation of unsteady phenomena such as combustion instabilities. As regards unsteady numerical analysis, direct numerical simulations have provided promising results thanks to the coupling of interface tracking or capturing methods for the primary atomisation process to Lagrangian methods for the description of the spray (Herrmann 2010, 2011, Kim & Moin 2011, Zuzio et al. 2016). These approaches are nevertheless not yet adapted to industrial reactive configurations. To this end, Large-Eddy Simulations (LES) seem more suitable. Indeed, LES based on the coupling of diffuse interface methods with either a Lagrangian (Zuzio et al. 2013) or an Eulerian (Le Touze 2015, Gaillard et al. 2016) spray description have proved their capabilities. In particular, the latter, in which the fully Eulerian formalism offers a natural and robust coupling to address primary atomisation, has been applied to simulate a stable cryogenic LOX/$\mathsf{GH_2}$ flame and reproduce a subcritical operating point of the MASCOTTE test bench (Murrone et al. 2014, Gaillard et al. 2016).

This last numerical strategy thus seems a priori adapted to deal with numerical studies of combustion instabilities in LRE under subcritical conditions. That is why it is retained in this paper and presented in section 2. Since the numerical strategy has initially been formulated without any acoustic modulation consideration, the first objective of the present contribution is to assess its behaviour once submitted to high-frequency acoustic modulation. On the basis of this evaluation, the second objective is to advance the understanding of the coupling mechanisms between transverse acoustic perturbations and atomised two-phase flows. To do so, it is chosen to consider a non-reactive case and to perform the numerical investigation on a fibre atomisation regime representative of LRE, with high levels of acoustic modulation. Under these specifications, the experimental configuration of Ficuciello et al.

(2017) is selected and simulated. Numerical specifications of the simulation are presented in section 3. To the authors' knowledge, this represents the first numerical study of the unsteady response of a non-reactive shear coaxial flow to transverse acoustic modulation under subcritical operating conditions. Some results without acoustic modulation are presented in section 4 as an illustration of the numerical strategy aforementioned. Qualitative comparisons of numerical results with experimental data are then discussed in next sections. The response of the liquid core to the acoustic forcing is analysed in section 5, while the effects of the acoustic modulation on the primary atomisation process and the dynamics of droplets are considered in sections 6 and 7 respectively. Note that quantitative comparisons with experiments do not fall within the scope of the present contribution and are planned for future work.

2 Coupling strategy for atomised two-phase flow simulations

2.1 General description

The numerical strategy retained in this work to simulate atomised two-phase flows is represented on figure 1. First, gas and liquid propellants are injected into the computational domain thanks to a *Separated Phases* Solver (SPS) dealing with the multi-species compressible Navier-Stokes equation system within an LES formalism, which is largely used in CFD codes based on the finite volume method. In the context of two-phase flows, the latter is nothing else than a diffuse interface model based on the homogeneous relaxation model, also referred to as the 4-equation model (Downar-Zapolski et al. 1996, Goncalvès 2014), with the difference that no mass transfer between the liquid and gas phases is considered. It is clear that more elaborated models such as a 7-equation model giving access to the temperature and the velocity of each phase would improve the modelling of liquid/gas/acoustics interactions in a reactive flow. Nevertheless, solving one momentum equation and one energy equation for each phase would require to define proper closures to the system and proper numerical schemes to solve it (Saurel & Lemetayer 2001). The use of a 4-equation model then represents a good compromise between the precision and the complexity of the two-phase flow modelling, especially considering the particular case of the simulation presented in this manuscript. Indeed, the two-phase flow simulated in this work is isothermal, which justifies the temperature relaxation hypothesis between both fluids considered by the 4-equation model. However, it is expected that the modelling of one velocity for each phase and the transport of geometric variables in order to access to subgrid scale evolutions of the interface between both fluids would be of great importance in the evaluation of two-

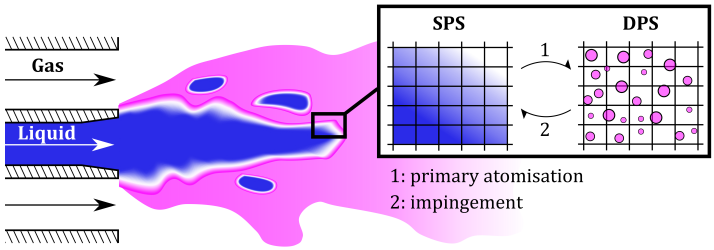

Figure 1: Schematic representation of the coupling strategy between the SPS and the DPS for the simulation of atomised two-phase flows.

phase flow/acoustics interactions. Therefore, such improvements could be considered in a near future for the numerical study of combustion instabilities.

At the coaxial injector outlet, the dense liquid phase is submitted to strong shear stresses due to the high surrounding gas injection velocity. Hence, this induces the atomisation of the dense phase and produces multiple liquid structures of different sizes and shapes. In theory, it would be possible to pursue the description of these structures with the SPS up to the smallest droplets, but this would require extremely refined meshes unsuitable for practical applications. Therefore, the choice is made in this work to fix the mesh to a reasonable refinement capable of describing large liquid structures and to use a statistical approach to deal with smaller ones that constitute the spray. A mass transfer from the SPS toward a kinetic-based Eulerian solver is then performed once the mesh becomes too coarse. Such *Dispersed Phase* Solver (DPS) is far less restrictive in terms of mesh refinement since it provides a subgrid modelling of the spray. In addition, a reverse transfer from the DPS to the liquid phase of the SPS accounts for a possible impingement of droplets onto the dense liquid core. This coupling strategy has been developed by Gaillard et al. (2016) and is implemented in Cedre, Onera's multi-physics simulation code (Refloch et al. 2011), with Cedre solvers Charme and Spiree as the SPS and the DPS respectively.

2.2 Governing equations

For the SPS, the system of governing equations can be written in vector form as:

$$\partial_t \boldsymbol{Q} + \boldsymbol{\nabla} \cdot (\boldsymbol{F} - \boldsymbol{\varphi}_D - \boldsymbol{\varphi}_C) = \boldsymbol{S}_G + \boldsymbol{S}_L + \boldsymbol{S}_F, \tag{1}$$

where ∂_t is the time partial derivative and $\boldsymbol{\nabla} \cdot ()$ is the divergence operator. $\boldsymbol{Q} = (\rho Y_g \ \rho Y_l \ \rho \boldsymbol{u} \ \rho e_t)^t$ is the vector of conservative variables, where Y_g and Y_l stand for the mass fraction of the gas and the liquid phases, while ρ, $\boldsymbol{u}$ and e_t correspond to the mixture density, velocity and specific total energy respectively. Note that the density of the mixture reads $\rho = \rho Y_g + \rho Y_l = \alpha_g \rho_g + \alpha_l \rho_l$, with ρ_g and ρ_l the densities of pure phases expressed through dedicated

equations of state, while $\alpha_g = \rho Y_g/\rho_g$ and $\alpha_l = \rho Y_l/\rho_l$ are the phase volume fractions. Since both fluids are injected at ambient temperature in this contribution, no thermal expansion is considered for the liquid phase. Considering only compressibility, the equation of state of the liquid thus reads $\rho_l(p) = \rho_0[1 + \beta_0(p - p_0)]$, where β_0 is the isothermal compressibility of the liquid at the reference state (ρ_0, p_0) and p is the local pressure of the mixture. Regarding the gaseous phase, the ideal gas law is retained. The thermodynamic closure of the system is then performed thanks to a thermal and mechanical equilibrium assumption (Goncalvès 2014, Chiapolino et al. 2017). In system (1), $\boldsymbol{F} = \boldsymbol{Q} \otimes \boldsymbol{u} + p(0\ 0\ \boldsymbol{I}\ \boldsymbol{u})^t$ is the vector of convective fluxes, with $\boldsymbol{I}$ the identity tensor and $\otimes$ the tensor product. The vector of laminar and turbulent diffusive fluxes reads $\boldsymbol{\varphi}_D = (0\ 0\ \boldsymbol{\tau}\ \boldsymbol{\tau} \cdot \boldsymbol{u} + \lambda \boldsymbol{\nabla} T)^t$, where λ and ∇T are the thermal conductivity and the temperature gradient of the mixture respectively. Note that classical Fourier's law is used to describe the laminar diffusion of heat even if it is not significant in this study, and that no mass diffusion is considered as the gas and liquid species belong to two different non-miscible phases. For the turbulence modelling, the Boussinesq's concept of eddy viscosity is adopted. The viscous stress tensor thus reads $\boldsymbol{\tau} = 2(\mu + \mu_t)\boldsymbol{D}$, where μ is the laminar dynamic viscosity of the mixture, μ_t is the turbulent dynamic viscosity and $\boldsymbol{D}$ is the deviator of the resolved symmetric strain rate tensor expressed as:

$$\boldsymbol{D} = \frac{1}{2}\left[\boldsymbol{\nabla} \otimes \boldsymbol{u} + (\boldsymbol{\nabla} \otimes \boldsymbol{u})^t\right] - \frac{1}{3}(\boldsymbol{\nabla} \cdot \boldsymbol{u})\boldsymbol{I}, \tag{2}$$

with $(\boldsymbol{\nabla} \otimes \boldsymbol{u})^t$ the velocity gradient tensor. The modelling of the turbulent viscosity inside the gaseous phase is performed thanks to the Wall-Damping version of the Smagorinsky (1963) model expressed as $\mu_t = \rho \min(C_s\Delta, \kappa d_w)^2 f_t$, where $C_s = 0.18$, as initially proposed by Lilly (1967), $\kappa = 0.41$ is the von Kármán constant, Δ is the size of the local control volume and d_w is the distance to the nearest wall. The turbulent frequency is expressed as $f_t = (2\boldsymbol{D} : \boldsymbol{D})^{1/2}$, where ():() is the double dot product of two tensors. In addition, the capillary fluxes in system (1) read $\boldsymbol{\varphi}_C = (0\ 0\ \boldsymbol{\tau}_C\ \boldsymbol{\tau}_C \cdot \boldsymbol{u})^t$, where $\boldsymbol{\tau}_C$ is the capillary stress tensor of the Continuum Surface Stress method (Lafaurie et al. 1994). The latter is a conservative alternative to the Continuum Surface Force approach of Brackbill et al. (1992), which provides a volume reformulation of surface tension forces. The capillary stress tensor is written as:

$$\boldsymbol{\tau}_C = \sigma \left\| \boldsymbol{\nabla} \alpha_l \right\| \left(\frac{\boldsymbol{\nabla} \alpha_l}{\left\| \boldsymbol{\nabla} \alpha_l \right\|} \otimes \frac{\boldsymbol{\nabla} \alpha_l}{\left\| \boldsymbol{\nabla} \alpha_l \right\|} - \boldsymbol{I} \right), \tag{3}$$

with σ the surface tension of the liquid-gas interface. Finally, $\boldsymbol{S}_G$ is the gravity source term written as $\boldsymbol{S}_G = (0\ 0\ \rho\boldsymbol{g}\ \rho\boldsymbol{g} \cdot \boldsymbol{u})^t$, with $\boldsymbol{g}$ the gravitational acceleration , while $\boldsymbol{S}_L$ and $\boldsymbol{S}_F$ are source terms referring to the coupling

between the SPS and the DPS. These coupling source terms will be discussed later.

Regarding the dispersed phase, its description at the highest level of accuracy is provided by the Williams-Boltzmann kinetic equation (WBKE) (Williams 1958), which describes at a mesoscopic level the evolution of the particle Number Density Function (NDF) in the phase space. However, the direct resolution of the WBKE being out of reach for practical applications (Murrone & Villedieu 2011), Eulerian methods rather solve transport equations derived from the WBKE for some particular moments of the NDF (see Emre et al. (2015) for a comprehensive review on Eulerian moment methods). An important part of the modelling is then to deal with the discretisation of the particle size distribution. Among the several approaches developed for this purpose in the framework of Eulerian moment methods, the sectional method (Greenberg et al. 1993, Laurent & Massot 2001) has been retained in the strategy of Gaillard et al. (2016) for its natural ability to account for phenomena that generate polydispersion, such as break-up. In the sectional approach, the size space is discretised into N_s contiguous *sections*, within which the shape of the particle size distribution has to be postulated. To this end, the affine-TSM (Two Size Moment) reconstruction of Sibra et al. (2017) was retained by Gaillard et al. (2016), as it seems to offer the best compromise between accuracy and computational cost. Finally, N_s systems of Eulerian equations are thus solved by the DPS, one for each section of the particle size distribution. They read in vector form (k denoting the number of a particular section):

$$\partial_t \boldsymbol{q}^k + \boldsymbol{\nabla} \cdot (\boldsymbol{q}^k \otimes \boldsymbol{v}^k) = \boldsymbol{s}_G^k + \boldsymbol{s}_L^k + \boldsymbol{s}_F^k + \boldsymbol{s}_B^k, \quad 1 \leq k \leq N_s, \tag{4}$$

with $\boldsymbol{q}^k = (\rho^k \ \rho^k \boldsymbol{v}^k \ n^k)^t$ the vector of conservative variables consisting of the bulk mass density, momentum and number density, with $\boldsymbol{v}^k$ the mean velocity vector of droplets in the section. The presence of droplets in a given control volume can also be assessed via the volume fraction of liquid in each section $\alpha^k = \rho^k/\rho_0$. Note that the configuration studied in this paper is quasi isothermal. Indeed, the gas and liquid phases are injected at the same temperature and temperature fluctuations due to acoustic perturbations are considered negligible. The temperature of droplets θ can then be considered constant and equal to the injection temperature of the liquid. As a result, no equation on the internal energy needs to be solved in the DPS. As for the SPS, the gravitational force is considered through a source term $\boldsymbol{s}_G^k = (0 \ \rho^k \boldsymbol{g} \ 0)^t$, while $\boldsymbol{s}_L^k$ and $\boldsymbol{s}_F^k$ are source terms referring to the coupling between the SPS and the DPS. The last term $\boldsymbol{s}_B^k$ stands for the exchange source term between the spray sections due to the fragmentation process.

2.3 Source terms

2.3.1 Coupling between the liquid phase and the spray ($\boldsymbol{S}_L$ and $\boldsymbol{s}_L^k$)

According to Gaillard et al. (2016), primary atomisation is modelled by a liquid mass transfer from the SPS to the DPS that reads:

$$S_a = \rho Y_l f_a \lambda_a, \tag{5}$$

where f_a is the characteristic frequency of the primary atomisation process and λ_a is an activation function. The atomisation process downstream coaxial injectors mainly depends on the local velocity difference between the gas and the liquid. In the context of homogeneous mixture models, where the whole mixture is described by only one mean velocity $\boldsymbol{u}$, the local velocity gradient can be used as an estimate. A simple choice is then to express the frequency of the primary atomisation process as $f_a = f_t$. In equation (5), the shape of λ_a is chosen in an empirical way to estimate the position of the interface but also to ensure numerical stability. This activation function thus reads $\lambda_a = 1 - \tanh(4Y_l^2)$ (see figure 2). Indeed, it is important that the transfer operates on the gaseous side of the diffuse interface where the mass of liquid in the SPS is negligible. Otherwise, the low compressibility of the liquid would induce significant pressure oscillations because the volume of droplets is not considered by the SPS. Finally, to perform the liquid mass transfer toward the DPS, the initial mean diameter D_a and velocity $\boldsymbol{v}_a$ of the droplets thus created have to be defined. Mechanisms responsible for the primary atomisation of the liquid core and the fragmentation of ligaments modelled by the SPS are directly related to the shape of liquid structures and the shear between the fluids. Therefore, the absence of information about the shape of the subgrid scale interface and the resolution of a single velocity for the mixture do not allow the formulation of a local and dynamic atomisation model. This could be handled in a near future thanks to the use of a 7-equation model combined with the transport of geometrical variables. With the current 4-equation model, the approach is to estimate constant and uniform average diameter D_a and velocity $\boldsymbol{v}_a$ thanks to experimental correlations whose evaluations are based on injection conditions (see section 3.4 for operating conditions simulated in this work). The Weber number of droplets for two-phase flows in fibre-type atomisation regime typical of liquid rocket engines is around 50 to 100 as soon as initial droplets are created because of the high gas velocity at the exit of the injector. The Weber number is then large enough so that the fragmentation of droplets quickly leads to downstream spray characteristics barely dependent on the initial droplet size. However, it is expected that the further local conditions deviate from injection ones the longer it will take for fragmentation to catch up on the initial error. As a consequence of this modelling, the mass transfer from the SPS is only operated toward one section of the DPS, namely $k = k_a$.

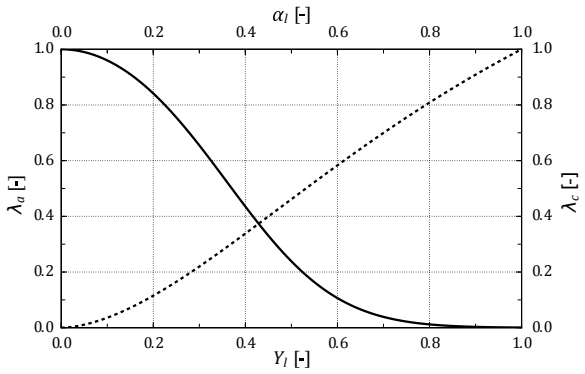

Figure 2: Activation functions for primary atomisation and impingement source terms. — λ_a ; - - λ_c.

In addition, a reverse liquid mass transfer from the DPS to the SPS accounts for the possible impingement of droplets onto the dense liquid core. This mass transfer is expressed for each section k as:

$$s_c^k = \rho^k f_c \lambda_c, \tag{6}$$

with f_c the characteristic frequency and λ_c the activation function. This impingement source term is only meant to avoid having spray in the dense core, and the frequency at which it occurs should be rigorously modelled. However, impingement of droplets with the liquid core occurs "at rest" along the two-phase flow interface in reality. But since the exact position of the interface is unknown in the 4-equation model, there is no reason for droplets to stop at the interface. The value $f_c = 1/\Delta t$, with Δt the integration time step, is thus considered large enough so that no droplets can pass into the liquid core. In regions where the physics is more complex, such as regions where droplets impinge with thin ligaments and rings, the value $1/\Delta t$ might be too crude. It is then preferred to deactivate the impingement source term in such regions, where the interface is known to be diffused, thanks to the activation function $\lambda_c = 1 - \tanh(-2 \log \alpha_l)$ (see figure 2).

According to the previous relations, the source terms $\boldsymbol{S}_L$ and $\boldsymbol{s}_L^k$ can be expressed as:

$$\boldsymbol{S}_L = \begin{pmatrix} 0 \\ -S_a + \sum_{k=1}^{N_s} s_c^k \\ -S_a \boldsymbol{v}_a + \sum_{k=1}^{N_s} s_c^k \boldsymbol{v}^k \\ -S_a \left[e_0 + \frac{1}{2} \boldsymbol{v}_a \cdot \boldsymbol{v}_a \right] + \sum_{k=1}^{N_s} s_c^k \left[e_0 + \frac{1}{2} \boldsymbol{v}^k \cdot \boldsymbol{v}^k \right] \end{pmatrix}, \tag{7}$$

and

$$\boldsymbol{s}_L^k = \begin{pmatrix} -s_c^k \\ -s_c^k \boldsymbol{v}^k \\ -\dfrac{s_c^k}{m^k} \end{pmatrix} \quad k \neq k_a, \qquad \boldsymbol{s}_L^{k_a} = \begin{pmatrix} S_a - s_c^{k_a} \\ S_a \boldsymbol{v}_a - s_c^{k_a} \boldsymbol{v}^{k_a} \\ \dfrac{S_a}{m(D_a)} - \dfrac{s_c^{k_a}}{m^{k_a}} \end{pmatrix}, \tag{8}$$

with $m^k = \rho_0 \pi {D^k}^3/6$ the mass of one droplet of diameter D^k. Since the configuration studied in this paper is quasi-isothermal and pressure is not considered in the DPS, the density and specific internal energy of the pure liquid in this solver can be assumed constant and respectively equal to reference state values ρ_0 and e_0. In the same way, $m(D_a) = \rho_0 \pi {D_a}^3/6$ is the mass of one droplet of diameter D_a.

2.3.2 Coupling between the gas phase and the spray ($\boldsymbol{S}_F$ and $\boldsymbol{s}_F^k$)

In the context of LRE applications, the density of the liquid phase is very high compared to the density of the gaseous phase and droplets may experience strong acoustic perturbations. Hence, in addition to gravity, the only forces acting on the dispersed phase are *a priori* drag and acoustic radiation forces.

The drag force experienced by a spherical isolated droplet of diameter D and velocity $\boldsymbol{v}$ in a medium of density ρ_g and velocity $\boldsymbol{u}$ can be calculated from the standard expression:

$$\boldsymbol{F}_D = \frac{1}{8}\pi D^2 \rho_g C_D \left\|\boldsymbol{u} - \boldsymbol{v}\right\| (\boldsymbol{u} - \boldsymbol{v}). \tag{9}$$

The drag coefficient C_D is estimated thanks to the correlation of Schiller & Naumann (1935) and depends on the droplet Reynolds number Re_p defined as:

$$\mathrm{Re}_p = \frac{\rho_g D \left\|\boldsymbol{u} - \boldsymbol{v}\right\|}{\mu_g}, \tag{10}$$

with μ_g the dynamic viscosity of the gaseous phase. Note that in the sectional approach, the drag force needs to be integrated over the size interval of each section k to get the total drag force of the section $\boldsymbol{F}_D^k$.

In addition, liquid sprays submitted to a transverse acoustic modulation experience an acoustic radiation force. Indeed, as mentioned by (King 1934), any object located in an acoustic field acts as an obstacle for the acoustic wave, thus inducing a wave reflection at its surface. The acoustic radiation pressure distribution around the object arising from this mechanism may lead to a resulting acoustic radiation force $\boldsymbol{F}_R$. Regarding the SPS, the acoustic radiation pressure distribution around the liquid structures is naturally rendered thanks to Navier-Stokes equations. However, the coupling

between the SPS and the DPS only intervene through source terms. Consequently, the ambient fluid does not take into account the volume occupied by the dilute spray and the local acoustic field around each spherical droplet is not simulated. Therefore, the acoustic radiation force has to be modelled in the DPS if one aims at taking into account its effect on the spray.

It is possible to evaluate *a priori* the deviation of droplets due to $\boldsymbol{F}_R$ in the configuration presented in this paper. To simplify, the acoustic field is supposed to be mono-harmonic. The time-averaging of the Newton's second law applied to one isolated droplet of constant mass m projected in the acoustic modulation direction $\boldsymbol{X}$ leads to:

$$m\overline{a_X} = \overline{F_R} + \overline{F_{D,X}}, \tag{11}$$

where a_X is the droplet acceleration in this direction, while $F_{D,X}$ is the X-component of the drag force. Assuming that every droplet undergoes periodic oscillations around the injection axis under the effect of the acoustic velocity, and that the mean deviation due to the acoustic radiation force is small, $\overline{F_{D,X}}$ can be considered null. Regarding $\overline{F_R}$, King (1934) formulated the time-averaged acoustic radiation force experienced by a small spherical droplet located in an intensity anti-node (IAN) of a standing acoustic field as:

$$\overline{F_R} = \frac{3}{4} m \left(\frac{p_{ac}}{\rho_g\, c}\right)^2 k_{ac}\, \eta\, \frac{1 + \frac{2}{3}(1-\eta)}{2+\eta}, \tag{12}$$

with c the speed of sound in the medium, $k_{ac} = 2\pi f_{ac}/c$ the acoustic wave number, p_{ac} and f_{ac} the amplitude and frequency of pressure fluctuations respectively and η the density ratio between the gas and the liquid. Hence, for the operating conditions presented in this contribution, the mean deviation ΔX of an isolated droplet injected with a null transverse velocity in an IAN of a standing acoustic field can be deduced by equations (11) and (12). This leads to $\Delta X = \overline{F_R}/(2m)\, t^2$, where t is the time elapsed since the injection of the droplet. According to the axial velocity of droplets in the present configuration once accelerated by the gas, each one needs 6 ms in average to span the study area. Therefore, the spray is deviated up to 40 µm at a maximum, which can be neglected compared to the transverse dimension of the spray of several dozen millimetres. As a result, the acoustic radiation force on droplets is not modelled in the DPS for the present contribution. Note that the evaluation of the mean deviation of droplets by $\boldsymbol{F}_R$ is however case dependent. The modelling of acoustic radiation forces on droplets may then still be necessary when dealing with different operating conditions. As a result, it has been implemented in our numerical tool in view of future work.

As a result, the source terms $\boldsymbol{S}_F$ and $\boldsymbol{s}_F^k$ referring to the coupling mech-

anisms between the gas phase and the spray can be expressed as:

$$\boldsymbol{S}_F = \begin{pmatrix} 0 \\ 0 \\ -\sum_{k=1}^{N_s} \boldsymbol{F}_D^k \\ -\sum_{k=1}^{N_s} \boldsymbol{F}_D^k \cdot \boldsymbol{v}^k \end{pmatrix}, \qquad \boldsymbol{s}_F^k = \begin{pmatrix} 0 \\ \boldsymbol{F}_D^k \\ 0 \end{pmatrix}. \tag{13}$$

2.3.3 Exchanges between the sections of the spray ($\boldsymbol{s}_B^k$)

The fragmentation of droplets due to the velocity differential with the gaseous phase is modelled at the scale of a single isolated droplet, and then formulated in the sectional formalism under the form of exchanges between the different sections. Indeed, droplets belonging to any section k are prone to break-up into smaller droplets whose size fall into the range of any inferior section. To estimate the physical properties of droplets after fragmentation, three key elements have to be evaluated: the fragmentation frequency ν_{fr} of a single mother droplet of diameter D_m and velocity $\boldsymbol{v}_m$, as well as D_{fr} and $\boldsymbol{v}_{fr}$, the mean diameter and velocity of daughter droplets thus created.

Following the model proposed by Pilch & Erdman (1987), the fragmentation frequency ν_{fr} depends on different break-up regimes, and is expressed as a function of the local Weber number $\mathrm{We} = \rho_g \left\|\boldsymbol{u} - \boldsymbol{v}_m\right\|^2 D_m/\sigma$. The model proposed by Wert (1995) is then used to provide D_{fr} as the Sauter mean diameter of the daughter droplets, depending on D_m, We and ν_{fr}. Finally, a zero-dissipation fragmentation is assumed, so that the velocity of daughter droplets $\boldsymbol{v}_{fr}$ equals to the velocity $\boldsymbol{v}_m$ of the mother droplet.

Once these three elements are evaluated, the fragmentation operator may be formulated and integrated over the size interval of each section k. For the sake of readability, the resulting expression of the fragmentation source term $\boldsymbol{s}_B^k$ is not presented in this paper, but more details are given by Dufour et al. (2003).

3 Geometry and numerical specifications

3.1 Computational domain and mesh

To investigate interaction mechanisms between acoustics and two-phase flows in injection conditions representative of those in LRE, the experimental configuration of Ficuciello et al. (2017), from CORIA laboratory, is simulated. The experimental test rig, represented on figure 3, consists in a cavity equipped with four speakers at the bottom and a coaxial injector at the top.

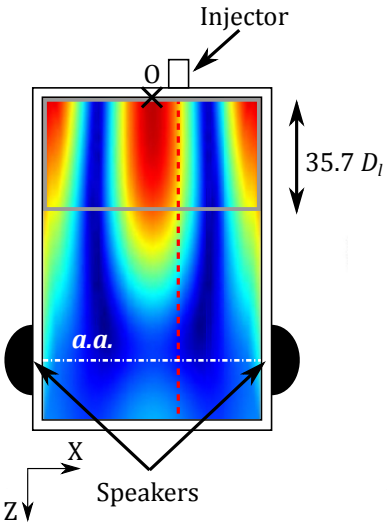

(a)

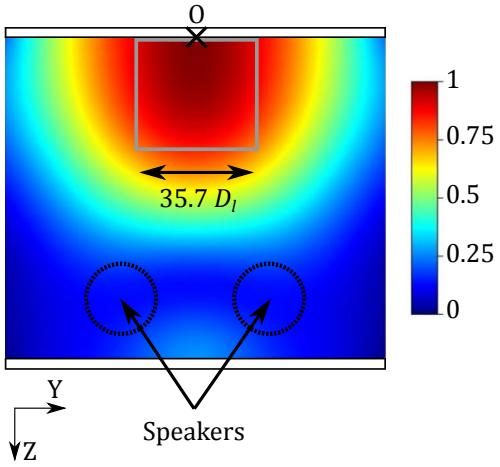

(b)

Figure 3: Experimental test rig of Ficuciello et al. (2017) coloured by normalised pressure amplitudes. (a) View containing the *a.a.* (b) View orthogonal to the *a.a.* — — Position of an IAN. ▭ Simulated part of the cavity.

In order to limit numerical costs, the numerical domain represented as a grey rectangle on figure 3 is reduced to a square section box of dimensions $64.3\,D_l \times 35.7\,D_l \times 35.7\,D_l$ with a $1.79\,D_l$-high coaxial injector at the top, D_l being the injection diameter of the central liquid flow at the exit of the injector. Thanks to signal processing, Ficuciello (2017) reveals that, in this domain, pressure fluctuations at the lateral walls mainly correspond to the

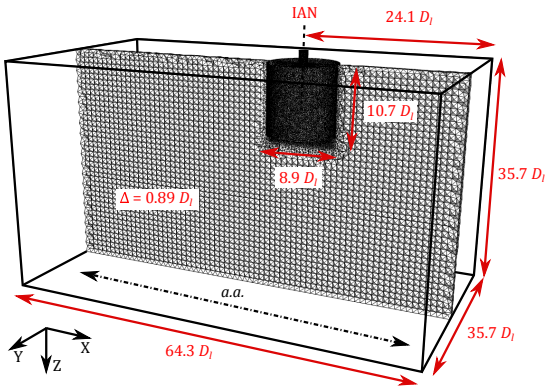

(a)

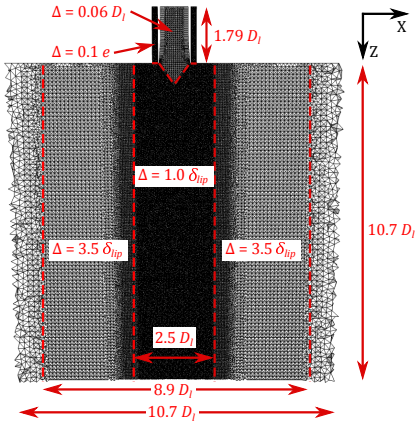

(b)

Figure 4: Mesh characteristics. (a) Far field 3D view. (b) Close-up view near the injector.

second, fourth and sixth transverse modes of the cavity of frequency around 1 kHz, 2 kHz and 3 kHz respectively, and that the experimental acoustic field can be considered as a plane standing acoustic wave. Note that in this configuration, the position of the injector can be set along the acoustic axis, mentioned as *a.a.* in the remainder of this paper. In order to maximise the number of acoustic effects observed in the numerical simulations, the injector is thus located at an IAN of the second transverse mode of the cavity (2T).

The computational mesh represented on figure 4 is made up with 28 million tetrahedra and prisms. The mesh is refined near the injector in a 10.7 D_l-high cylinder of diameter 2.5 D_l with a constant element size in order to capture dense liquid structures and external vortices downstream the liquid core, but also to capture main instabilities developing and propagating at the surface of the liquid core and resulting in its atomisation. More precisely, the mesh refinement is defined to ensure the capture of longitu-

dinal and transverse instabilities due to shear stresses between both fluids at the exit of the injector. In the particular conditions simulated in this manuscript, wave lengths of such instabilities are $\lambda_{/\!/} = 14.0\,\delta_{lip}$ and $\lambda_{\perp} = 5.6\,\delta_{lip}$ respectively according to Marmottant & Villermaux (2004), where δ_{lip} is the injector lip thickness. Furthermore, Baillot et al. (2009) observed Faraday instabilities at the surface of the liquid core once it is submitted to acoustic perturbations, which can impact primary atomisation mechanisms. In the case simulated in this manuscript, the wave length of these instabilities is $6.3\,\delta_{lip}$. Therefore, the mesh is refined near the liquid core to a constant element size of δ_{lip}, which represents 5 to 6 cells for the discretisation of the smallest wave length $\lambda_{\perp}$. A second $10.7\,D_l$-high cylindrical box, of greater diameter $8.9\,D_l$, is filled with $3.5\,\delta_{lip}$-size elements on average in order to assure the resolution of at least 80 % of the turbulent kinetic energy in the gas (Pope 2000). Based on the same criterion, the injector is filled with $0.06\,D_l$-size tetrahedra and four layers of $0.03\,D_l$-high prisms inside the central tube. Considering e as the thickness of the external coaxial channel, the numerical mesh is refined in the annular tube down to $0.1\,e$ for tetrahedra and $0.05\,e$ for prisms. This results in two tetrahedra within the injector lip thickness, which is not adequate to capture the smallest vortices created at the injector lip. However, refining the mesh in this particular area would considerably increase numerical cost. It is known that the influence of vortices at the exit of the injector on the flame behaviour is significant (see Varoquié et al. (2002)). Nevertheless, in the non-reactive case simulated in this contribution, the influence of these vortices on the atomisation of the liquid core is expected to be of less importance. This is supported by section 4.2, where a good agreement is found between the liquid core length obtained by the numerical simulation and the experimental correlations of Villermaux (1998). In the rest of the domain, the mesh refinement is set to minimise the numerical dissipation of acoustic waves. More precisely, the cut-off frequency of the mesh defined as $f_c = c/(\mathrm{PPW}\,\Delta)$, with c the speed of sound in the medium, PPW the minimum number of points per wavelength required and Δ the mean size of cells, has been set to a value of 3.6 kHz which is 1.2 times bigger than the highest acoustic frequency to simulate associated to the sixth transverse mode of the cavity. According to Langenais et al. (2018), the minimum number of points to be used with Cedre code when using second order numerical schemes for the discretisation of an acoustic wave is $\mathrm{PPW} = 20$. This leads to a mesh refinement of $0.89\,D_l$.

3.2 Operating and boundary conditions

The operating conditions investigated in the present contribution have been selected in collaboration with Coria in order to meet with both experimental and numerical requirements. As a result, the liquid mass flow rate has been increased compared to operating conditions studied by Ficuciello

et al. (2017) in order to limit computational costs. Water and air are both injected at atmospheric pressure and a temperature of 300 K. This gives rise to a momentum flux ratio J = 4 and a gaseous Weber number $\mathrm{We}_g = 490$, according to the following expressions:

$$\mathrm{J} = \frac{\rho_g U_g^2}{\rho_l U_l^2} \quad ; \quad \mathrm{We}_g = \frac{\rho_g U_g^2 D_l}{\sigma}, \tag{14}$$

where U_g and U_l are the air and water velocities at the exit of the coaxial injector. According to Lasheras & Hopfinger (2000), this corresponds to a fibre-type atomisation regime representative of LRE operating under subcritical conditions.

Constant and homogeneous injection velocities and temperatures are imposed at the inlet boundaries of the injector. Adiabatic no-slip conditions are prescribed at injector walls and lip, as well as at the top-wall of the cavity.

3.3 Acoustic forcing

Two cases are studied and compared to each other in experiments and numerical simulations: one with an acoustic modulation, namely the modulated case (MC), and the other one without any, namely the non modulated case (NMC).

Regarding the MC, the higher the SPL is the greater the response of the two-phase flow will be. Therefore, the maximum sound pressure level (SPL) that experiments can sustain has been prescribed. For the experimental configuration of Coria considered in this manuscript, this maximum SPL value is 166 dB. The raw experimental pressure signal p' measured at a Pressure Anti-Node (PAN) of the 2T mode near the top wall of the cavity is plotted on figure 5 over one acoustic period. From this figure, it is clear that the acoustic field contains multiple harmonics causing the deformation of the pressure signal. More precisely, signal processing showed that 98.3 % of the acoustic energy of the raw experimental signal is comprised into the frequency range [0 Hz ; 3,000 Hz], and more precisely in the 2T, 4T and 6T modes of the cavity. Therefore, only these three modes are considered for the numerical reproduction of the experimental acoustic field. To this end, the way that has been retained in this work comes from Rey et al. (2005), except that relaxed boundary conditions are used instead of Navier–Stokes Characteristic Boundary Conditions (NSCBC). The acoustic forcing methodology thus consists in continuously prescribing pressure fluctuations $p'(t)$ on lateral boundaries located on both sides of the acoustic axis, following the form:

$$p'(t) = \sum_{i=1}^{3} p_{ac,\,i} \sin\left(2\pi f_{ac,\,i} t + \psi_{ac,\,i}\right), \tag{15}$$

where $f_{ac,\,i}$, $p_{ac,\,i}$ and $\psi_{ac,\,i}$ are the frequency, amplitude and phase of each harmonic i. These parameters are evaluated thanks to a discrete Fourier

transform on the experimental signal of figure 5 and are given in table 1. Since the width of the cavity corresponds to the wave length of the 2T mode, pressure fluctuations at both boundaries must be in phase in order to get a standing acoustic wave in the domain. As concerns the lateral and bottom numerical boundaries parallel to the *a.a.*, these correspond to free-flowing limits in the experiment. It is thus chosen to prescribe on these boundaries an unsteady and heterogeneous pressure profile that complies with pressure fluctuations in the cavity along the *a.a.*.

Relaxed boundary conditions used in the Separated Phases Solver can be expressed as :

$$\frac{\partial \boldsymbol{W}_l}{\partial t} = \boldsymbol{f}_{rel} \cdot (\boldsymbol{W}_m - \boldsymbol{W}_l), \tag{16}$$

where $\boldsymbol{W} = (p\, T\, \boldsymbol{u}\, Y_g)^t$ and where l and m indices respectively stand for effective and target values at the boundary. The target vector $\boldsymbol{W}_m$ is defined as $\boldsymbol{W}_m = \left(p'(t)\, \widetilde{T}\, \widetilde{\boldsymbol{u}}\, \widetilde{Y_g}\right)^t$, with $\widetilde{T}$, $\widetilde{\boldsymbol{u}}$ and $\widetilde{Y_g}$ the reconstructed values of T, $\boldsymbol{u}$ and Y_g at the limit from the internal fields in the numerical domain, while $p'(t)$ is the prescribed pressure fluctuation. In formulation (16), $\boldsymbol{f}_{rel}$ corresponds to a tensor made of relaxation frequencies of each variable contained in $\boldsymbol{W}$ and is defined as :

$$\boldsymbol{f}_{rel} = \begin{pmatrix} f_{rel,p} & 0 & 0 & 0 \\ 0 & f_{rel,T} & 0 & 0 \\ 0 & 0 & f_{rel,u}\, \boldsymbol{I} & 0 \\ 0 & 0 & 0 & f_{rel,Y} \end{pmatrix} = \begin{pmatrix} \dfrac{1}{\Delta t} & 0 & 0 & 0 \\ 0 & \widetilde{f} & 0 & 0 \\ 0 & 0 & \widetilde{f}\, \boldsymbol{I} & 0 \\ 0 & 0 & 0 & \widetilde{f} \end{pmatrix}, \tag{17}$$

with Δt the integration time step and $\widetilde{f}$ a relaxation frequency. This means that each variable contained in $\boldsymbol{W}_l$ is relaxed toward their target value at frequency $\widetilde{f}$, except for pressure which is relaxed at the integration time step frequency. Note that reflection characteristics of boundary conditions directly depend on the value of the relaxation frequency $\widetilde{f}$. More particularly, it can be shown that the magnitude $|R|$ and phase φ of the complex reflection coefficient R can be expressed as :

$$|R|^2 = \frac{1}{1 + \left(\dfrac{4\pi f_{ac}}{\widetilde{f}}\right)^2} \qquad \text{and} \qquad \varphi = \pi - \arctan\left(\frac{4\pi f_{ac}}{\widetilde{f}}\right). \tag{18}$$

Hence, we see that if reflecting boundary conditions are used (*i.e.* $\widetilde{f} \to \infty$), then the reflected wave will be out of phase with the incident acoustic wave, thereby preventing to get a standing wave in the numerical domain. It is thus necessary to use non-reflecting conditions. Therefore, it is chosen to prescribe a relaxation frequency $\widetilde{f} \approx 12\,\text{Hz}$ so that the maximum reflection coefficient magnitude is 10^{-3} for any acoustic wave of frequency higher than the 2T mode frequency.

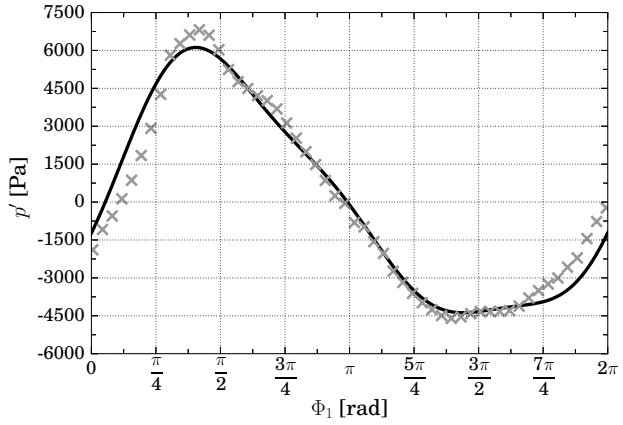

Figure 5: Pressure fluctuations at a PAN of the cavity. × Raw experimental signal and — numerical reconstruction for the acoustic forcing.

i	Mode	$f_{ac,\,i}$ [Hz]	$p_{ac,\,i}$ [Pa]	$\psi_{ac,\,i}$ [rad]
1	2T	≈ 1000	5135	0
2	4T	$2\ f_{ac,\,1}$	887	5.44
3	6T	$3\ f_{ac,\,1}$	555	4.97

Table 1: Characteristics of the acoustic signal at a PAN.

In the NMC, the cavity boundaries orthogonal to the *a.a.* are replaced with adiabatic no-slip conditions in order to represent the lateral panels in the experiment, while the other acoustic forcing boundaries are set to constant pressure conditions.

3.4 Modelling parameters, numerical schemes and simulation strategy

As mentioned in section 2.3.1, the modelling of the primary atomisation requires to postulate properties of the created droplets. To do so, the physical analysis of Marmottant & Villermaux (2004), linking the diameter and the velocity of created droplets to the injection velocities of gas and liquid flows, is used. For the present operating conditions, this approach gives rise to the following parameters: $D_a = 200\,\mu\text{m}$ and $\|\boldsymbol{v}_a\| = 3.5\,\text{m.s}^{-1}$. Note that coalescence between droplets is not taken into account in the present contribution. As a result, droplets issued from primary atomisation are created into the spray section containing the biggest droplets, *i.e.* $k_a = N_s$. The spray size distribution is divided into $N_s = 3$ sections for a good compromise between accuracy and numerical cost. For the sake of simplicity, these three sections are mentioned as *small*, *medium* and *big* sections in the present paper. Their upper bounds in terms of droplet diameter are respectively 50 µm, 150 µm

and 300 µm.

As concerns numerical methods, both the SPS and the DPS are based on a cell-centred finite volume approach on general unstructured meshes. Numerical fluxes are computed by means of upwind numerical schemes in both solvers together with second-order reconstructed values at the faces centroids thanks to the multislope MUSCL method (Le Touze et al. 2015). Furthermore, an operator splitting technique is used with dedicated explicit second-order time-stepping schemes.

Both numerical simulations MC and NMC are performed from the same initial time t_0 at which the two-phase field is established. For both simulations, a time scale based on the acoustic period T_{ac} of the 2T mode of the cavity is chosen in order to facilitate comparisons between both simulations, despite the absence of acoustic modulation during the NMC. During the physical time simulated in MC, the dense liquid phase and the gaseous flow travel a distance of $5\,D_l$ and $312\,D_l$ respectively. This corresponds to about 0.5 and 29 convective times along the refined $10.7\,D_l$-high cylinder of figure 4. The spray, with a vertical speed comprised between U_l and U_g, travels between 2.5 and 7.5 times this distance depending on the size of droplets. The physical time simulated in MC also corresponds to $23\,T_{ac}$. Even if this simulation time is not long enough to achieve average convergence for the liquid phase, it permits to establish the two-phase flow under acoustic modulation. Hence, a complete analysis of the transient behaviour of the liquid from the beginning of the acoustic forcing is performed. Regarding the NMC, a physical time equivalent to $18\,T_{ac}$ is simulated.

The numerical simulation of both cases required a total of 4.3 MhCPU on Intel Haswell processors, with typical runs involving 1,000 MPI processes.

4 Two-phase flow simulation without any modulation

4.1 Instantaneous shape of the two-phase flow

In order to get a first overview of the numerical strategy and thus facilitate upcoming interpretations, a qualitative comparison of experimental and numerical results without acoustic modulation is performed. Figure 6 shows snapshots of the two-phase flow near the exit of the injector for experiments and numerical simulations. Experimental images (see figure 6a) are acquired thanks to high-speed back-light visualisations at a frequency of 6.2 kHz. Regarding numerical snapshots (see figure 6b), the visualisation of the dense liquid phase solved by the SPS and its diffuse interface model requires to fix a critical value of liquid volume fraction. Indeed, the interface between the gas ($\alpha_l = 0$) and the liquid ($\alpha_l = 1$) is spread over the mesh. Dense liquid structures are thus represented on figure 6b with a black 3D isosurface of

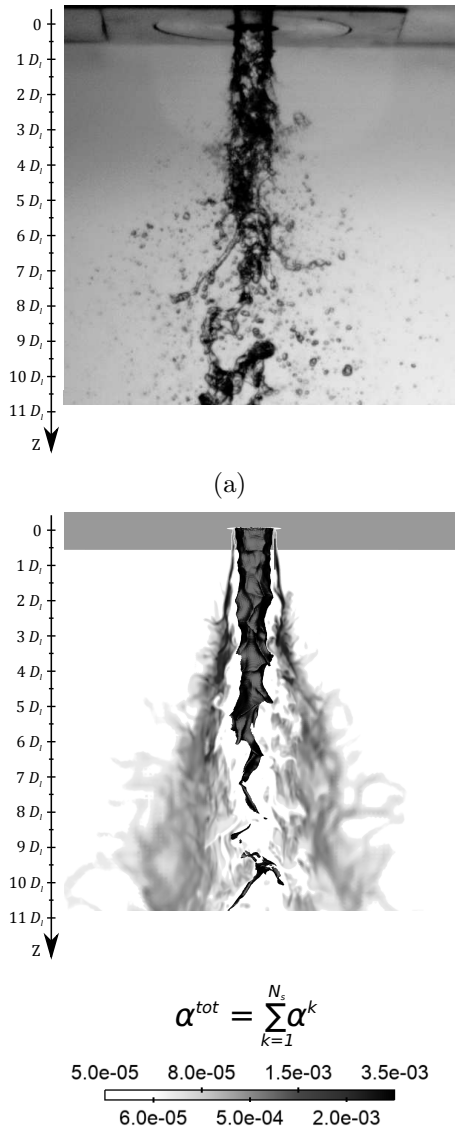

Figure 6: (a) Experimental and (b) numerical snapshots of the two-phase flow near the injector exit (NMC).

$\alpha_l = 0.99$, which will be denoted $\alpha_{l,0.99}$ in the sequel. As regards the spray, the presence of droplets is represented thanks to a longitudinal slice of spray volume fraction $\alpha^{tot} = \sum_k \alpha^k$ in grey scale.

On both images, the liquid core can be observed as a long dark structure that extends from the exit of the injector. Both snapshots reveal longitudinal and transverse hydrodynamic instabilities growing at its surface under the action of shear stresses due to the cocurrent gas flow. These instabilities

can be captured by the numerical simulation thanks to the mesh refinement described in section 3.1. As stated by Marmottant & Villermaux (2004), these instabilities are the ones that control the primary atomisation process and the spray angle in fibre-type atomisation regime. These instabilities then result in the detachment of large liquid structures at its tip which propagate along the injection axis. In addition, the peeling of the liquid core results in the creation of droplets around it both in experimental and numerical images. These droplets are thus convected downward by the gaseous stream and expand radially to form a conical spray whose angle exclusively depends on the momentum flux ratio J according to Villermaux (1998), which means that surface tension does not play a part in the opening of the spray. From this macroscopic comparison between numerical and experimental results, it appears that the coupling strategy of section 2 is able to retrieve the qualitative topology of the liquid flow.

4.2 Mean shape of the central liquid core

More quantitative comparisons are necessary to assess the numerical reproduction of the two-phase flow without acoustic modulation. Unfortunately, the presence of the spray in experimental back-light images impedes to perform any measurement of the liquid core length for the operating conditions simulated in this paper. However, experimental correlations obtained in the past can be used as reference. Villermaux (1998) conducted experiments to characterise the time-averaged probability of presence of the central liquid phase downstream the injector outlet thanks to a laser-induced fluorescence technique. A mean dye concentration C was thus measured along the jet axis and normalised by the injected concentration C_0. For the dilution length L_x, defined as the distance from the injector outlet to reach a given dilution level $C/C_0 = x$, the authors found the following correlations:

$$\frac{L_{1.0}}{D_l} = 6\, J^{-\frac{1}{2}}, \quad \frac{L_{0.5}}{D_l} = 12\, J^{-\frac{1}{2}}. \tag{19}$$

To compare with these correlations, the dilution level along the jet axis can be assessed in the NMC thanks to the time-averaged liquid volume fraction $\overline{\alpha_l}$. A planar cut of $\overline{\alpha_l}$ containing the injection axis is plotted on figure 7. The time-average is performed over a time range equivalent to 18 acoustic periods.[1] From this two-dimensional field, it is possible to extract the length of isolines $\overline{\alpha_{l,\,1.0}}$ and $\overline{\alpha_{l,\,0.5}}$. For the present operating conditions where J = 4, the numerical results $L_{1.0} = 3.51\, D_l$ and $L_{0.5} = 5.95\, D_l$ are in good agreement with experimental correlations predicting $L_{1.0} = 3.0\, D_l$ and $L_{0.5} = 6.0\, D_l$. This contributes to the validation of the coupling strategy of section 2 for the simulation of two-phase flows without acoustic perturbation.

[1] It should be remembered that the number of acoustic periods T_{ac} of the 2T mode is used as reference even for the NMC.

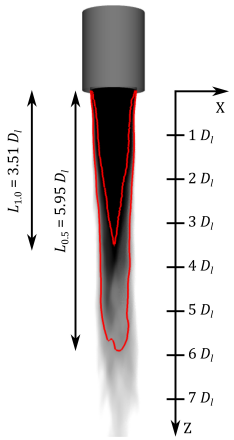

Figure 7: Longitudinal slice coloured by $\overline{\alpha_l}$ in grey scale (NMC). — Isolines of $\overline{\alpha_{l,\,1.0}}$ and $\overline{\alpha_{l,\,0.5}}$.

The next step of this work is to evaluate the ability of the code to retrieve the effects of the acoustic modulation on the jet. First, the flattening of the liquid core by acoustic radiation pressure and the induced decrease of its length are analysed in section 5. Then, the impact of the acoustic modulation on the primary atomisation process is studied in section 6. Finally, effects of acoustic perturbations on the shape and dynamics of the spray are examined in section 7.

5 Response of the liquid core to the acoustic forcing

5.1 Flattening of the liquid core

As mentioned above, the isosurface $\alpha_{l,\,0.99}$ can be used to represent liquid structures solved by the SPS. After a physical time equivalent to 18 acoustic periods, such isosurfaces are represented on figures 8a and 8b for the NMC and the MC respectively. In addition, transversal cuts of liquid volume fraction are displayed in grey scale at different distances from the injection plane in order to better visualise the change of liquid core shape. From a certain distance downstream the injection, it is clear that acoustic perturbations tend to flatten the liquid core in the $\boldsymbol{X}$ direction (*i.e.* the *a.a.*) and stretch it in the spanwise $\boldsymbol{Y}$ direction.

This phenomenon is difficult to observe on experimental images for the present operating conditions due to the presence of multiple ligaments and droplets hiding the liquid core. However, it has already been observed by Ficuciello et al. (2017) for other operating conditions with lower momentum flux ratio and gaseous Weber number (J = 2.8 and $\mathrm{We}_g = 20$) but with the same acoustic modulation as the one considered in this manuscript. Back

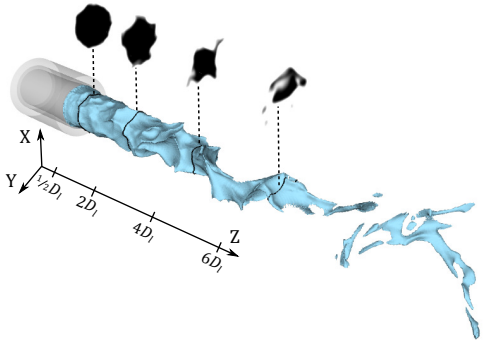

(a)

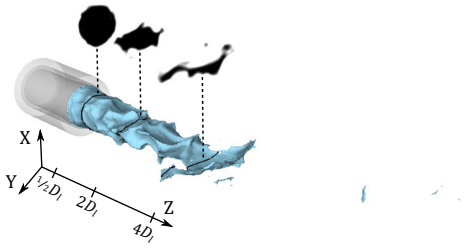

(b)

Figure 8: Liquid core representation with blue isosurfaces of $\alpha_{l,\,0.99}$ and transversal cuts of α_l in grey scale (black: $\alpha_l = 1$; white: $\alpha_l = 0$). (a) NMC and (b) MC at $t = 18\,T_{ac}$.

then, the authors explained the deformation of the liquid core by considering the acoustic radiation pressure distribution $p_{rad}(\theta)$ around the liquid jet. Based on the work of King (1934), Zhuk (1986) and Wu et al. (1990), Ficuciello (2017) expressed the dimensionless acoustic radiation pressure distribution $p^*_{rad}(\theta)$ around any cylindrical-like liquid core of radius R located in a mono-harmonic standing acoustic wave of wave number k_{ac}. When the cylinder is small enough to consider $k_{ac}R \ll 1$, the distribution reads:

$$\begin{aligned} p^*_{rad}(\theta) =& \frac{p_{rad}(\theta)}{\overline{P}}, \\ =& \frac{\cos^2(k_{ac}h)}{4} \\ &+ \frac{\sin^2(k_{ac}h)}{(1+\eta)^2}\Big(\eta^2\cos^2\theta + (2\eta-1)\sin^2\theta\Big) \\ &- \frac{k_{ac}R\sin(2k_{ac}h)}{2(1+\eta)}\Big(\sin\theta\sin(2\theta)(1-\eta) + \cos\theta\Big). \end{aligned} \tag{20}$$

In this expression, h is the distance along the $a.a.$ between the axis of the cylinder and any PAN, θ is the angular coordinate around the cylinder and $\eta = \rho_g/\rho_l$. Moreover, the acoustic radiation pressure is normalised by $\overline{P} =$

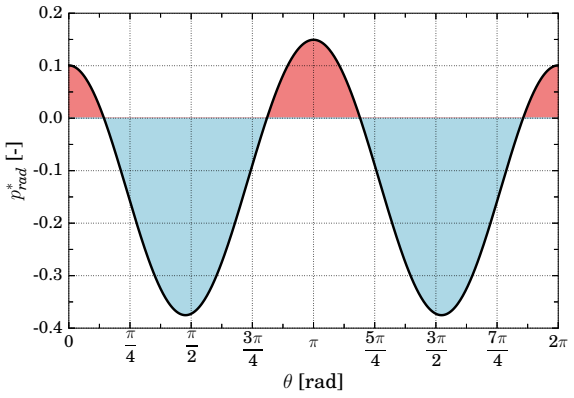

Figure 9: Theoretical p^*_{rad} distribution around a cylinder located at an IAN of a standing acoustic field. Red zones: compression effect; blue zones: suction effect.

$p^2_{ac}/(\rho_g c^2)$, p_{ac} being the acoustic pressure amplitude. As an illustration, the theoretical distribution of $p^*_{rad}(\theta)$ around the cylinder is plotted on figure 9 for the particular case addressed in this paper (*i.e.* $k_{ac}h = \pi/4$ for an injection at an IAN and $k_{ac}R = 4.9 \times 10^{-2}$). Since $\overline{P}$ depends on p^2_{ac}, the effect of harmonics can be neglected for simplification reasons. The acoustic radiation pressure is then only calculated for the 2T mode of the cavity. It can be seen on figure 9 that the acoustic radiation pressure exhibits maximum positive values along the acoustic axis ($\theta \equiv 0 \mod \pi$) resulting in a compression of the liquid, and minimum negative values in the perpendicular direction ($\theta \equiv \pi/2 \mod \pi$) resulting in a suction of the liquid. For the present operating conditions, where $\overline{P} \approx 185\,\text{Pa}$, the acoustic radiation pressure drop defined as $\Delta p_{rad} = p_{rad,\,max} - p_{rad,\,min} \approx 90\,\text{Pa}$ exceeds the Laplace pressure drop due to surface tension, *i.e.* $\Delta p_{Lap} = 2\sigma/D_l \approx 24\,\text{Pa}$. As a consequence, acoustic radiation stresses overcome the surface tension, thus resulting in the flattening of the liquid core observed on figure 8b.

A quantitative investigation of the liquid core deformation is performed by measuring the flattening parameter f of the transverse liquid interface profile at different distances Z from the injection plane as:

$$f = \begin{cases} \dfrac{a}{b} - 1 & \text{if } a < b, \\ 1 - \dfrac{b}{a} & \text{otherwise,} \end{cases} \tag{21}$$

with parameters a and b defined on figure 10. According to this definition, f is confined in the $[-1,1]$ range and equals to zero for perfectly circular shapes. A flattening along the *a.a.* is characterised by positive values of f, while negative values reflect a flattening in the orthogonal direction. The time evolution of f is plotted on figure 11 at four distances from the injection

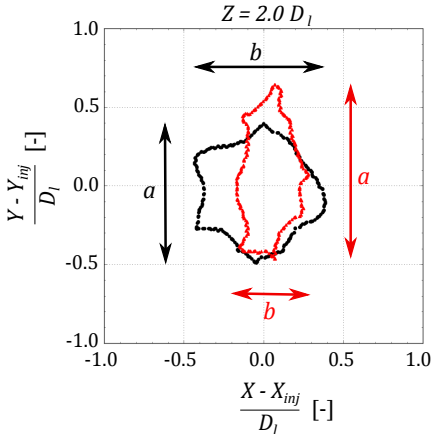

Figure 10: Instantaneous transversal cuts of the liquid interface for $\alpha_{l,0.99}$. (X_{inj}, Y_{inj}): injection centre coordinates. •• NMC ; •• MC.

plane ($D_l/2$, $2\,D_l$, $3\,D_l$ and $4\,D_l$) for both the NMC and the MC. During the NMC, the evolution of f seems to be centred around zero whatever the position but still exhibits fluctuations increasing with the distance to the injection plane. This reflects a progressive deformation of the liquid jet under aerodynamic constraints induced by the gaseous flow. However, since the two-phase flow displays an axial symmetry in the case without acoustic modulation, the liquid deformation does not statistically show any preferred direction. As regards the MC, the flattening of the core actually depends on the time spent by the liquid particles inside the acoustic field. As a result, the flattening parameter keeps a quasi null value at the exit of the injector ($Z = D_l/2$), but progressively deviates from zero beyond a distance of $2\,D_l$ to reach strictly positive values associated with a flattening process along the *a.a.*, as observed on instantaneous transversal cuts of figure 8b. In addition, the value around which f is established increases with the distance to the injection plane. These observations are in accordance with experimental results of Baillot et al. (2009), for which the flattening of the liquid core does not occur right at the exit of the injector.

5.2 Decrease of the liquid core length

In addition to the flattening of the liquid core, figure 8 seems to reveal a drastic decrease of its length once submitted to the acoustic modulation. The time evolution of the liquid core length L_{lc} normalised by D_l is thus plotted on figure 12 for both the NMC and the MC, with different threshold values on α_l. If we first consider the NMC, drops of L_{lc} are noticed at low frequency, whatever the retained threshold value. This phenomenon has already been observed experimentally by Hardi et al. (2014) in transcritical operating conditions. For both sub- and transcritical conditions, this

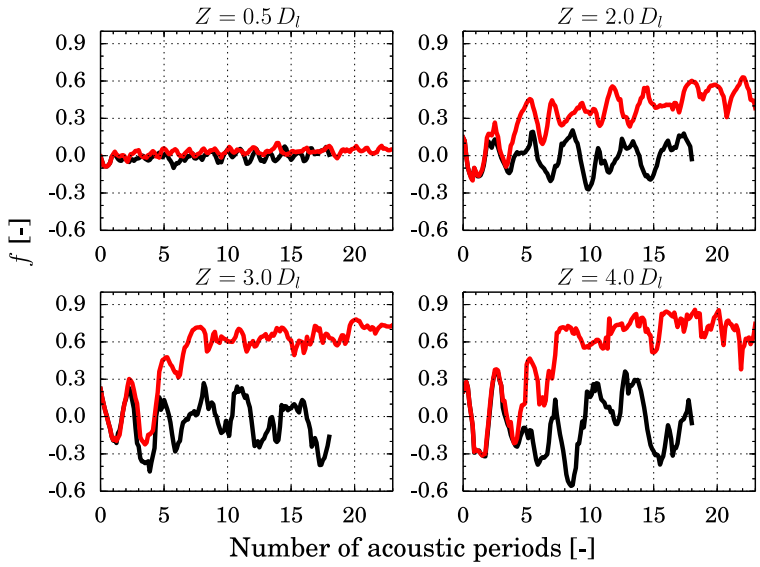

Figure 11: Time evolution of the flattening parameter f at different distances Z from the injection plane. — NMC ; — MC.

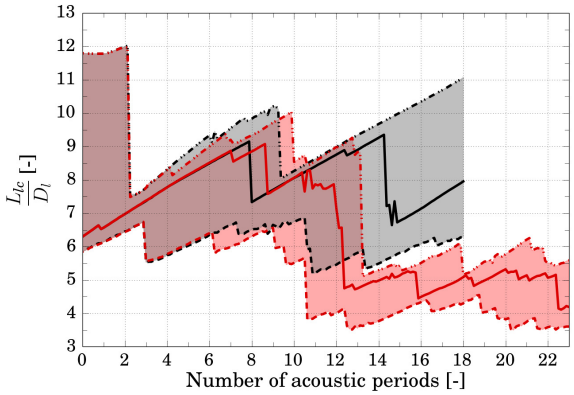

Figure 12: Time evolution of the liquid core length. -·-·- $\alpha_{l,\,0.9}$, — $\alpha_{l,\,0.99}$ - - $\alpha_{l,\,1.0}$ (black: NMC ; red: MC).

growth-and-detachment behaviour results from the natural disintegration of the dense core into large dense structures, even if the two cases present strong differences of surface tension and density ratio between the two injected fluids. Note that L_{lc} strongly depends on the threshold value chosen for α_l. Indeed, since the interface is diffused in the SPS, a liquid fragment that appears to be just torn from the liquid core can still be considered as part of the jet for a smaller value of α_l. Quantitative comparisons between instantaneous experimental and numerical measurements are consequently not straightforward.

Regarding the response of the liquid core in the MC, the evolution of L_{lc} can be split in two : a transitory and an established phase. The transitory phase starts at the beginning of the plot, when the acoustic forcing is set, and ends after approximately 9 to 13 acoustic periods, depending on the value of α_l. During this time interval, the liquid core length keeps a similar evolution to that of the NMC, with only few differences at the end. After that, the length suddenly drops whatever the value of α_l. From this point, the trend of L_{lc} seems to be established, with a growth-and-detachment behaviour similar to that of the NMC. If we consider the threshold value $\alpha_{l,0.99}$, the drop of L_{lc} occurs after 12 acoustic periods and reaches about 40 % of the initial length. Such behaviour has been noticed both numerically and experimentally in transcritical operating conditions by Hakim, Ruiz, Schmitt, Boileau, Staffelbach, Ducruix, Cuenot & Candel (2015) and Hardi et al. (2014), and has been attributed by last authors to a transverse shedding mechanism of the dense phase due to gas oscillations. For sufficiently high acoustic amplitudes, large pockets of oxygen were stripped away from the dense core along the *a.a.* by the transverse acoustic velocity, without giving the opportunity to large structures to detach from the tip of the dense core. In subcritical conditions, a drop of the liquid core length under acoustic modulation has also been observed (Baillot et al. 2009). However, no stripping of the liquid core occurred because of the higher density ratio between the gas and the liquid than in transcritical conditions. To explain the decrease of L_{lc} in subcritical conditions, we thus refer to figure 13 representing the liquid core for the NMC and the MC just before (see figure 13a) and after (see figure 13b) a drastic decrease of the liquid core length in the MC (*i.e.* around $t = 12\,T_{ac}$). In addition, transversal cuts of the liquid interface are plotted at $Z = 4.5\,D_l$, corresponding to the distance at which operates the cut of the liquid core. It can be noticed on figure 13a that the flattening effect analysed in the previous section actually pinches the interface of the liquid core until its thickness reaches a critical value, hence causing the core break-up. From then on, the core length is established whatever the threshold value on α_l and remains shortened as long as acoustic perturbations are set. It is not evident to determine if this break-up mechanism intervenes in transcritical conditions since the only plane of visualisation in experiments of Hardi et al. (2014) corresponds to the one containing the *a.a.*

The diffuse interface method in the SPS is thus able to reproduce the flattening of the liquid core and the decrease of its length observed experimentally due to acoustic perturbations. In addition, the analysis of the transitory behaviour of the liquid flow gives the opportunity to advance the understanding of the link between acoustic radiation pressure and the cut of the liquid core. This is of first importance since this may have a drastic impact on the flame length in LRE and thus participate to the thermoacoustic coupling.

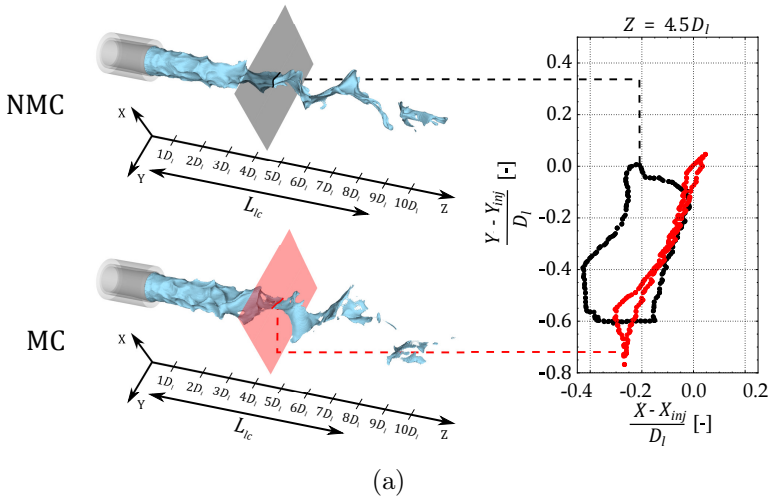

(a)

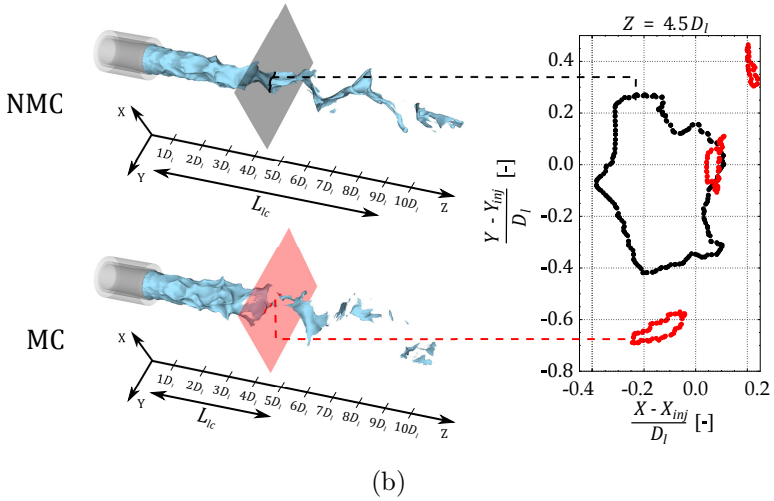

(b)

Figure 13: Isosurfaces of $\alpha_{l,0.99}$ with transversal cuts of the liquid interface at $Z = 4.5\,D_l$ (•• NMC ; •• MC). (a) $t = 11.5\,T_{ac}$, (b) $t = 12.5\,T_{ac}$.

6 Impact of the modulation on the primary atomisation process

6.1 Response of the Separated Phases Solver

The main goal of coaxial injectors used in LRE is to assist the atomisation of the liquid phase and maximise the amount of interface shared with the gaseous phase. Indeed, the evaporation of the liquid phase and the intensity of the combustion are thus promoted, which leads to high-efficiency propulsion systems. Since the local combustion dynamics has a direct impact on the thermoacoustic coupling, it is therefore of great interest to investigate the evolution of the liquid interface area once submitted to acoustic

perturbations. To characterise the interface, the interfacial area density Σ, defined as the amount of liquid surface per unit of volume, can be used. In the scope of diffuse interface models such as the one used in the SPS, Sun & Beckermann (2004) specified that the resolved interfacial area density may be locally defined as $\Sigma_{SPS} = \|\boldsymbol{\nabla}\alpha_l\|$. The total interfacial area density in a given volume of interest Ω is then defined as:

$$\Sigma_{SPS,\Omega} = \frac{\sum_{V_c \in \Omega} \|\boldsymbol{\nabla}\alpha_l\| \, |V_c|}{|\Omega|}, \tag{22}$$

where $|V_c|$ and $|\Omega|$ denote the volumes of a mesh element V_c and of the domain of interest Ω. Based on this definition, the time evolution of $\Sigma_{SPS,\Omega}$ is plotted on figure 14 for both the NMC and the MC, with Ω corresponding to the volume of revolution presented on figure 4b. Since both cases start from an established solution, the value of $\Sigma_{SPS,\Omega}$ at the beginning of the plot is not null. In the NMC, it can be seen that $\Sigma_{SPS,\Omega}$ does not depart much from its time-averaged value. On the contrary, in the MC, $\Sigma_{SPS,\Omega}$ starts to progressively increase after approximately one acoustic period, *i.e.* right after the establishment of the standing acoustic wave. Then, after approximately 13.5 acoustic periods, $\Sigma_{SPS,\Omega}$ starts to decrease slowly. The increase of $\Sigma_{SPS,\Omega}$ is actually due to the flattening of the liquid core resulting in the expansion of the liquid interface in the direction orthogonal to the *a.a.* and thus to the increase of the liquid core surface. In addition, after approximately 12 acoustic periods, the pinching of the liquid by acoustics promotes the break-up of the liquid core into smaller structures at its tip, hence increasing the amount of interface between both fluids. During this process, the liquid structures thus created experience themselves acoustic radiation pressure, which tends to promote their break-up as well. As a result, the amount of interface is supposed to keep increasing and then stabilise once the size of liquid fragments reaches an established value due to the equilibrium between acoustic radiation pressure and surface tension. However, for sufficiently high acoustic perturbations, the liquid core breaks up into structures too small to be correctly described by the local mesh refinement. In such a case, the volume fraction is spatially diffused which results in a local decrease of $\|\boldsymbol{\nabla}\alpha_l\|$. This actually explains the drop of resolved interfacial area density observed in figure 14 after the decrease of the liquid core length due to acoustic radiation pressure. Indeed, this can be observed on figure 15 where slices of $\|\boldsymbol{\nabla}\alpha_l\|$ are compared at two different instants: 1) when the interfacial area density of the MC is maximum ($t = 13.5\,T_{ac}$) and 2) after $\Sigma_{SPS,\Omega}$ has decreased ($t = 22\,T_{ac}$). In the MC, a strong diffusion of the liquid structures is noticed at the tip of the liquid core, leading to the homogenisation of $\|\boldsymbol{\nabla}\alpha_l\|$.

It can also be seen, by comparing the field of $\|\boldsymbol{\nabla}\alpha_l\|$ on figure 15a to figures 15b and 15c (or equivalently the field of α_l on figure 15d to figures

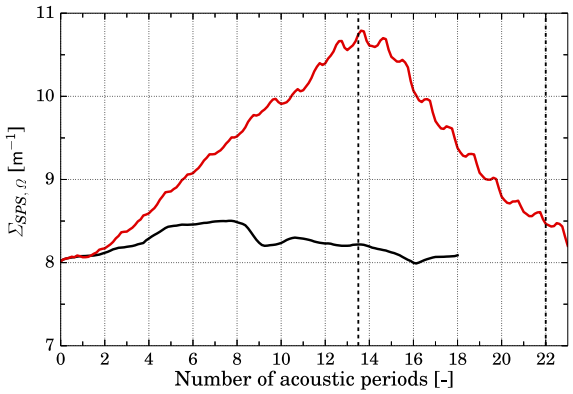

Figure 14: Time evolution of the resolved interfacial area density in the SPS. — NMC ; — MC.

15e and 15f), that the liquid expansion in the direction orthogonal to the *a.a.* is far greater in the MC than in the NMC. This is actually also due to the flattening of the liquid core and the promotion of its stripping by acoustic radiation pressure. Indeed, as observed by Ficuciello et al. (2017), once the jet is flattened, small liquid ligaments are torn from the central core and ejected in the orthogonal direction to the *a.a.*. The SPS seems thus able to render the expansion of the liquid mass in this direction. Note that since the numerical mesh is too coarse in this region to discretise such small liquid structures, the gradient of the liquid volume fraction is diffused. In such highly diffused zones, the loss of information about the interface shape and position as well as the fact that only the mixture velocity is solved may deteriorate the evaluation of interactions between the gas and the liquid in the SPS. This is a well known limitation of the model. To quantify the amount of liquid that expands, let us define highly diffused zones by the double condition $\|\boldsymbol{\nabla}\alpha_l\| < 100$ and $\alpha_l < 0.99$. Based on this definition, it appears that approximately 15 % of the total mass of liquid in the SPS is found in these highly diffused zones in the MC, compared with only 3 % in the NMC. At this point, it is worth noting that this mass of liquid is not necessarily transferred to the DPS since it essentially corresponds to ligaments. A way to gain accuracy in these zones for the evaluation of interactions between the gas and the liquid without any additional mesh refinement would be to solve a transport equation of Σ_{SPS} with specific source terms adapted to the subgrid modelling of the break-up process induced by shear stresses and the acoustic radiation pressure. Hence, the subgrid interfacial area density would bring useful information to enhance the modelling of the liquid behaviour. The use of an advanced modelling of the two fluids in the SPS giving access to their own velocities in the interface could also improve the overall strategy.

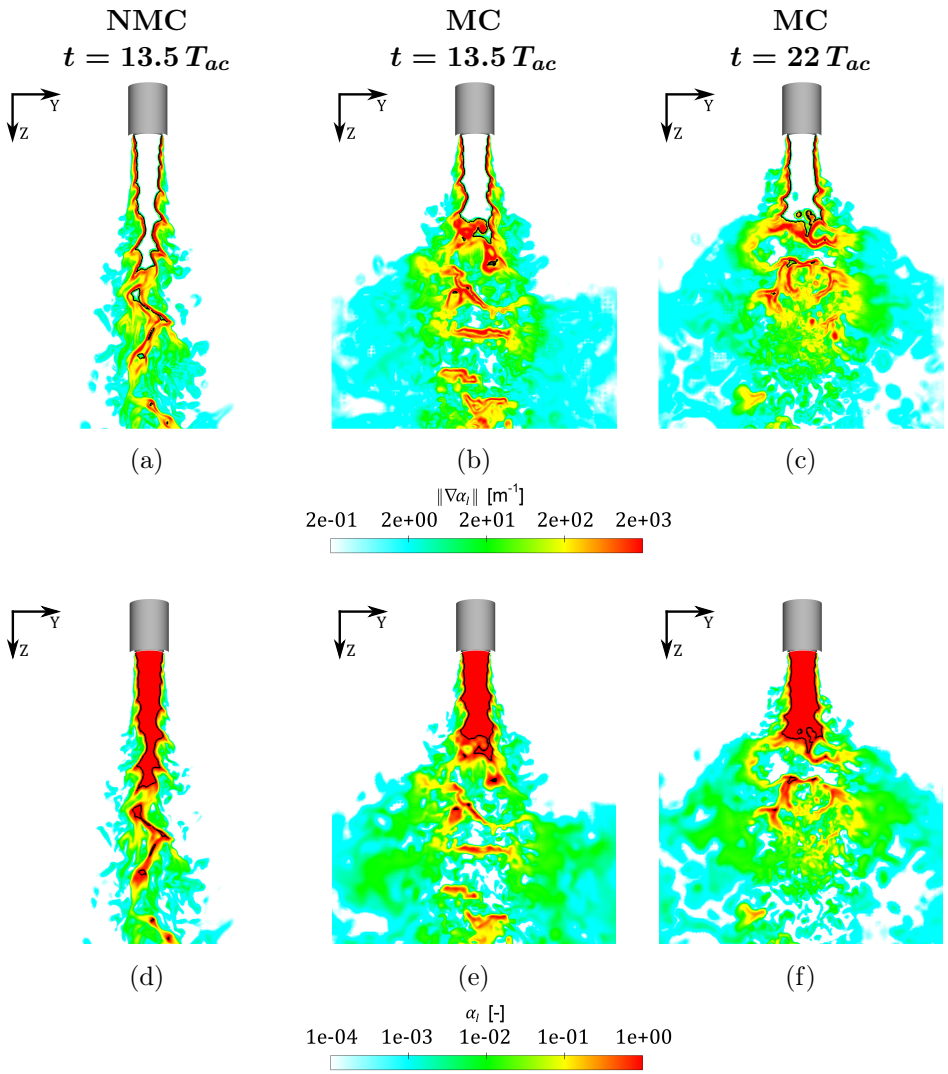

Figure 15: Slices orthogonal to the *a.a.* coloured by $\|\boldsymbol{\nabla}\alpha_l\|$ for (a) (b) (c), and by α_l for (d) (e) (f). — Isolines of $\alpha_{l,0.99}$.

Regarding future reactive simulations, both the fragmentation of ligaments at the tip of the liquid core and the transverse expansion of the liquid in the direction orthogonal to the *a.a.* under acoustic perturbations are expected to bring more liquid structures in high-temperature zones, which would induce a greater evaporation of the liquid. To model such phenomenon and its influence on combustion, an evaporation model would have to be formulated in the SPS.

6.2 Response of the Dispersed Phase Solver

The primary atomisation process is naturally rendered by the SPS as long as the mesh refinement permits to resolve the interface dynamics and topology. Otherwise, the coupling strategy with the DPS takes over to provide a modelling of the process at the subgrid scale level. Therefore, to complete the previous analysis, the amount of liquid interface accounted for in the DPS has to be measured as well. According to its definition, the interfacial area density of the spray in a given volume Ω reads $\Sigma_{DPS,\Omega} = \mathcal{S}_\Omega/|\Omega|$, with $\mathcal{S}_\Omega$ the total surface of droplets in the volume. By introducing the total volume of droplets $\mathcal{V}_\Omega$, $\Sigma_{DPS,\Omega}$ may be written as $\Sigma_{DPS,\Omega} = \alpha_\Omega^{tot}\mathcal{S}_\Omega/\mathcal{V}_\Omega$, with $\alpha_\Omega^{tot} = \sum_{V_c\in\Omega}\alpha^{tot}|V_c|/|\Omega|$ the volume fraction of droplets in Ω, all sections k considered. In addition, the introduction of the Sauter mean diameter of the spray $D_{32,\Omega}$, which corresponds to the diameter of a single droplet with the same ratio $\mathcal{V}/\mathcal{S}$ as the whole spray, leads to :

$$\Sigma_{DPS,\Omega} = 6\frac{\alpha_\Omega^{tot}}{D_{32,\Omega}}. \tag{23}$$

Based on this definition, time evolutions of $\Sigma_{DPS,\Omega}$, α_Ω^{tot} and $D_{32,\Omega}$ are plotted on figure 16 for both the NMC and the MC. As stated before, Ω corresponds to the volume of revolution presented on figure 4b.

After a numerical transitory phase equivalent to one acoustic period due to a change of numerical parameters for both cases, the trend of $\Sigma_{DPS,\Omega}$ quickly converges around a value of $3\,\mathrm{m}^{-1}$ for the NMC, whereas it increases all along the simulation for the MC. According to equation (23) and figures 16b and 16c, this increase is due to a growth of α_Ω^{tot}, and consequently the total mass of droplets, while the Sauter mean diameter $D_{32,\Omega}$ remains quasi constant. This reflects an intensification of the mass transfer from the SPS toward the DPS once the jet is submitted to acoustic perturbations. The liquid expansion observed on figure 15 associated to the transverse ejection of small liquid ligaments in the SPS actually occurs in a zone where shear stresses are important due to the high-velocity gas flow. Since the primary atomisation source term (equation (5)) depends on Y_l but not on $\|\boldsymbol{\nabla}\alpha_l\|$, the mass transfer from the SPS toward the DPS increases in this zone even if the resolved component of the interfacial area density diminishes in the SPS.

For a better quantification of the phenomenon, the net mass transfer rate per unit volume between the SPS and the DPS is defined as:

$$S_{net} = S_a - \sum_{k=1}^{N_s} s_c^k, \tag{24}$$

while the mean net mass transfer rate over the whole volume Ω reads:

$$S_{net,\Omega} = \frac{\sum_{V_c\in\Omega} S_{net}|V_c|}{|\Omega|}. \tag{25}$$

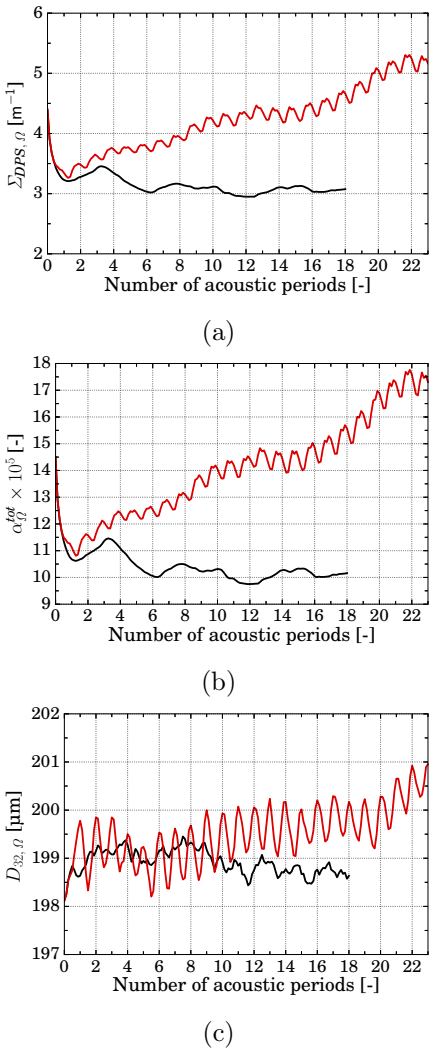

Figure 16: Time evolution of (a) the interfacial area density in the DPS, (b) the total volume fraction of the spray and (c) the Sauter mean diameter. — NMC ; — MC.

Computing the time-average of $S_{net,\Omega}$ over 13 acoustic periods leads to $\overline{S_{net,\Omega}} = 13.14\,\mathrm{kg.s^{-1}.m^{-3}}$ under acoustic modulation, against $9.42\,\mathrm{kg.s^{-1}.m^{-3}}$ in the NMC. This increase of approximately 40 % is significant and may have a drastic impact on the combustion stability in typical LRE configurations.

The previous analysis thus demonstrates the ability of the coupling strategy to render the increasing trend of the primary atomisation process by acoustic radiation stresses. A quantitative validation of the model will be performed once experimental data will be available on this particular operating conditions.

7 Dynamics of the spray under acoustic modulation

7.1 Spray angle modification

An additional impact of acoustic perturbations on the two-phase flow is the drastic expansion of the spray angle in the direction orthogonal to the *a.a.*, as observed by Baillot et al. (2009) and Ficuciello et al. (2017). In order to quantify this mechanism in the current simulations, the spray angle in the aforementioned direction has been defined as shown on figure 17a and reads:

$$\gamma_+ = \frac{\sum_{V_c \in \Lambda_+} \gamma\, \alpha^{tot}\, |V_c|}{\sum_{V_c \in \Lambda_+} \alpha^{tot}\, |V_c|}, \qquad \gamma_- = \frac{\sum_{V_c \in \Lambda_-} \gamma\, \alpha^{tot}\, |V_c|}{\sum_{V_c \in \Lambda_-} \alpha^{tot}\, |V_c|}, \tag{26}$$

where γ corresponds to the angle between the injection axis and the segment connecting the injector lip to the centre of any control volume V_c, while α^{tot} is the local volume fraction of droplets, all sections k considered. If we denote Λ the set of control volumes intersected by the plane orthogonal to the a.a. and containing the injection axis, then Λ_+ and Λ_- are the domains of positive and negative Y-coordinates respectively. The spray angle is thus weighted by the local volume of droplets, and consequently their mass. Contrary to usual experimental measurements based on back-light images, this numerical measurement technique does not necessitate to fix a value on the minimum occurrence ratio to consider. The time evolution of the spray angle in the direction orthogonal to the *a.a.* is represented on figure 17b for the NMC and the MC. A significant increase of the angle is noticed on both directions once submitted to acoustic perturbations, while it remains quasi constant throughout the NMC. After approximately 10 acoustic periods, the angle converges around $\pm$ 20° which corresponds to twice the value without acoustic modulation.

To explain this phenomenon, figure 18 represents two-dimensional fields of $\overline{S_{net}}$ and of the time-averaged liquid mass fraction $\overline{Y_l}$ for the NMC and the MC, the time-average being performed over 13 acoustic periods. On this figure, the transverse expansion of the liquid mass fraction is clearly visible. As explained in section 6, this corresponds to ligaments being ripped from the liquid core under acoustic perturbations but too small to be correctly discretised by the mesh. Since the primary atomisation source term (equation (5)) depends on Y_l, the location of mass transfer toward the DPS consequently tends to depart from the injection axis, which in turn directly impacts the spray angle. This can be retrieved on figure 18, where zones of positive $\overline{S_{net}}$ follow the expansion of the isoline $\overline{Y_l} = 0.4$. Therefore, this demonstrates the ability of the coupling strategy between the SPS and the DPS to render the increasing trend of the spray angle once submitted to acoustic perturbations. However, comparisons with experimental data are

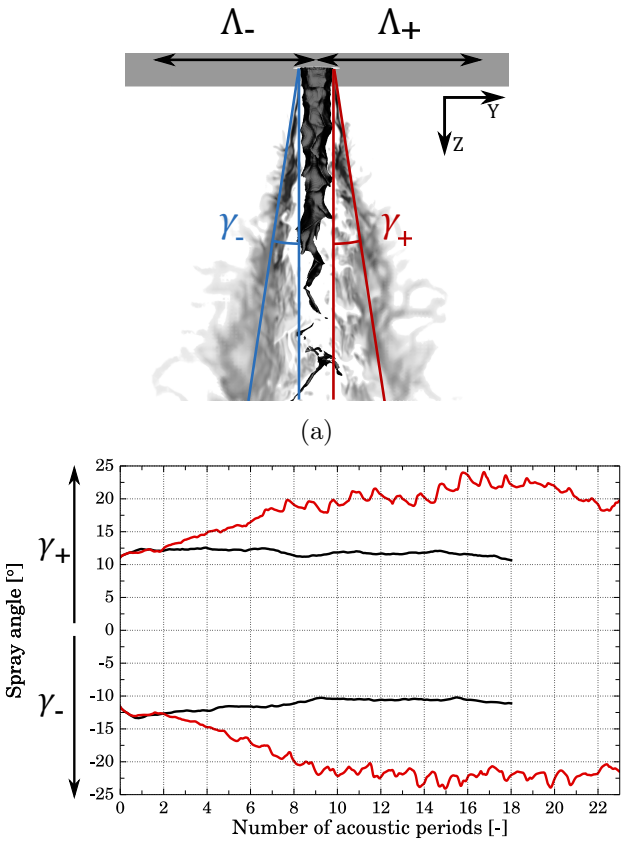

Figure 17: (a) Definition and (b) time evolution of the spray angle in the direction orthogonal to the *a.a.*. — NMC ; — MC.

needed to adjudicate on the modelling precision of the phenomenon. Indeed, the diffusion of the interface in the SPS might result in an overestimate of the volume taken by ligaments around the liquid core, and consequently distort the radial expansion of the spray.

7.2 Transverse oscillations

The last item of this study concerns the response of the spray to the acoustic velocity. Due to compression and decompression mechanisms, the propagation of acoustic waves results in both pressure and velocity fluctuations in the medium. In the case of the standing acoustic wave simulated in this paper, the acoustic velocity can be expressed along the *a.a.* $\boldsymbol{X}$ as :

$$v'(X,t) = \sum_{i=1}^{3} (-1)^{i+1} \frac{p_{ac,i}}{\rho_g\, c} \cos\left(2\pi f_{ac,i} t + \psi_{ac,i}\right) \sin\left(k_{ac,i}\, X\right), \qquad (27)$$

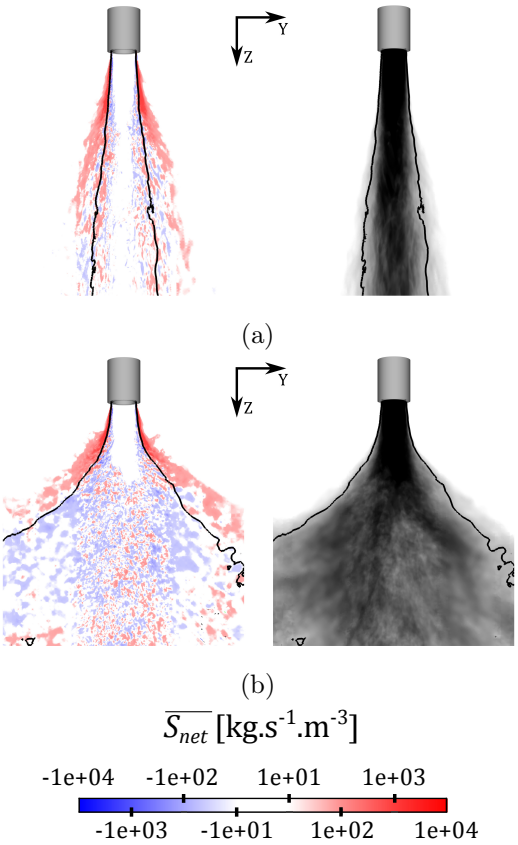

Figure 18: Slices orthogonal to the *a.a.* coloured by $\overline{S_{net}}$ on the left and $\overline{Y_l}$ on the right. (a) NMC, (b) MC. — Isolines $\overline{Y_l} = 0.4$.

with $k_{ac,\,i} = 2\pi f_{ac,\,i}/c$ the acoustic wave number of each harmonic i. According to acoustic parameters given in table 1, the theoretical acoustic velocity amplitude at the injection position, *i.e.* the IAN located at $X = \lambda_{ac,\,1}/8 = c/(8f_{ac,\,1})$ with $\lambda_{ac,\,1}$ the wave length of mode 2T, is equal to approximately 8 m/s. This amplitude is more than 10% of the gas injection velocity and results in a transverse periodic movement of the gas. According to Méry et al. (2013), these velocity fluctuations may induce periodic oscillations of droplets around their injection axis and contribute to the coupling between flames and acoustics in a reactive case. Therefore, it is of first interest to be able to reproduce this transverse movement of the spray in numerical simulations. In order to measure the global response of the spray to the acoustic velocity, the spatial mean velocity of droplets in direction $\boldsymbol{X}$ is calculated

as:

$$\langle v_X^k \rangle_\rho = \frac{\sum\limits_{V_c \in \Xi} v_X^k \, \rho^k \, |V_c|}{\sum\limits_{V_c \in \Xi} \rho^k \, |V_c|} \tag{28}$$

where $\langle \, \rangle_\rho$ refers to the spatial mean weighted by the local density of droplets ρ^k, v_X^k is the transverse velocity of droplets of section k in the control volume V_c and Ξ is a set of control volumes intersected by a given transverse plane of constant Z-coordinate. Measurements are performed over two transverse slices Ξ located at distances of $Z = 0.2\,D_l$ and $Z = 2.7\,D_l$ from the injection plane respectively.

Figure 19 represents Discrete Fourier Transforms (DFT) of the time evolution of $\langle v_X^k \rangle_\rho$ over 18 acoustic periods for small, medium and big spray sections, for both transverse slices. At $Z = 0.2\,D_l$, droplets undergo transverse oscillations at the three modulation frequencies during the MC, whatever the spray section. As expected, the amplitudes of oscillation for each mode depend on their inertia: the greater the inertia, the smaller the transverse movement amplitude. This response mechanism is retrieved thanks to the coupling strategy between the gas and the spray solvers, through the drag force term $\boldsymbol{F}_D^k$ (see section 2.3.2). Regarding the transverse slice at $Z = 2.7\,D_l$, it appears that droplets do not respond significantly to the 4T and 6T acoustic modes. In addition, the amplitude of oscillation at the main frequency $f_{ac,1}$ is greater compared to the one at $Z = 0.2\,D_l$, whatever the droplet size (+300 % for small droplets ; +100 % for medium and big droplets). This difference in the response amplitude is mainly caused by the fact that, due to their inertia, droplets do not reach instantly their maximum oscillation amplitude. Therefore, the oscillation of droplets seems to significantly depend on their size. Since the flame response in LRE configurations directly depends on the dynamics of the spray, the description of the droplet size distribution by the DPS as well as the coupling between the gas flow and the spray through drag terms appear essential in the framework of CFD analysis of combustion instabilities.

8 Conclusion

In this work, the unsteady simulation of a non-reactive air-assisted liquid jet submitted to a high-frequency transverse acoustic modulation has been performed. The methodology of Gaillard et al. (2016) has been retained to describe the dynamics of the whole jet in an Eulerian framework, from injection to atomisation processes. This methodology consists in the coupling between a diffuse interface method for the simulation of large liquid structures, and a kinetic-based Eulerian model for the description of droplets. It is known from experiments that acoustic waves may have a great impact on the

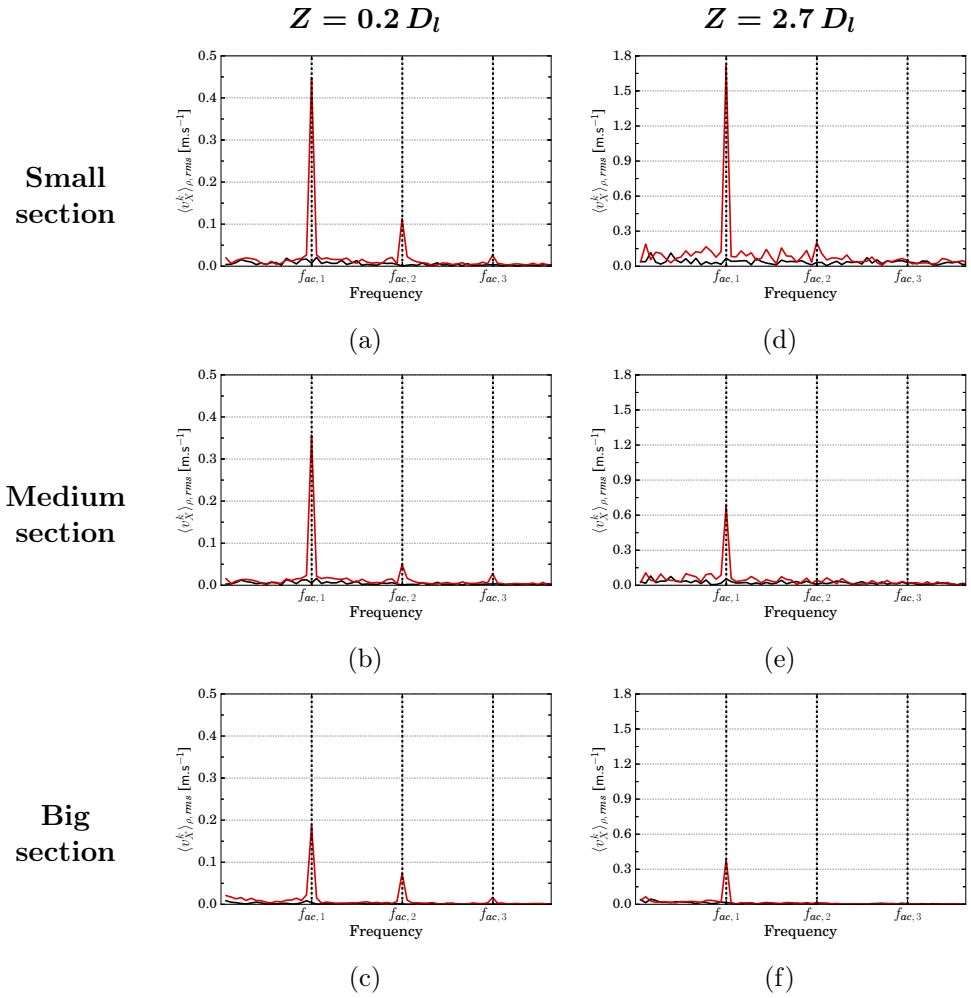

Figure 19: DFT of $\langle v_X^k \rangle_\rho$ at two distances Z from the injection plane and for the three spray sections. ━ NMC ; ━ MC.

spray properties. The aim of the present contribution was thus to evaluate the ability of the coupling strategy to render all the response mechanisms of two-phase flows submitted to transverse acoustic perturbations, typical of what actually occurs in liquid rocket engines under unstable operating conditions. The selected configuration corresponds to the one of Ficuciello et al. (2017), which already brought much information on the response of two-phase flows under such acoustic forcing. Two simulations have been performed in this paper. The first one has been carried out without any acoustic modulation and used as reference, while the second one considers the jet under transverse acoustic forcing. The results of these two simulations have thus been compared to each other as well as to experimental data available in the literature.

From these simulations, it appears that the flattening of the liquid core by the heterogeneous profile of acoustic radiation pressure observed experimentally is well retrieved by the diffuse interface method. This flattening process gives rise to an enhanced atomisation of the liquid core associated to a release of small liquid structures at its tip and in the plane orthogonal to the acoustic axis. Due to the mesh refinement, this change in the primary atomisation process results in a diffusion of the liquid volume fraction and may contribute to a loss of precision in the transport of the liquid structures thus created. To gain accuracy, the resolution of an additional transport equation of the interfacial area density could be adequate. However, even though information about the interface position and shape are lost, it is found that the current formulation of the mass transfer source term between both solvers is adapted to render the intensification of the primary atomisation. In addition, the expansion of the liquid structures by acoustic radiation stresses directly results in the increase of the spray angle in the plane orthogonal to the acoustic axis. This phenomenon has already been observed in the literature and may have a great impact on the flame response in reactive cases. Finally, the transverse periodic motion of droplets under the action of the acoustic velocity is also captured thanks to the coupling between the gaseous phase and the spray through drag forces. Significant differences in the amplitudes of droplet oscillations have been noticed depending on their size. Since the flame response in liquid rocket engines is directly related to the dynamics of the spray, the description of the droplet size polydispersion by the spray solver turns out to be essential in the numerical study of combustion instabilities.

Future work is planned to complete the present contribution with quantitative comparisons to ongoing experimental measurements. In addition, the same kind of numerical simulation will be performed in a reactive framework in order to improve understanding of the driving mechanisms of HF combustion instabilities in subcritical operating conditions. These simulations are also expected to provide a basis for an accurate low-order modelling of phenomena.

Acknowledgments

This work is supported and co-supervised by Cnes the French Space Agency and was granted access to the HPC resources of Cines under allocations 2016-c20162b7710 and 2017-A0022B07710 made by Genci. We gratefully thank Coria for sharing data as well as experience. The on-going work will be the occasion to maintain the joint effort between both labs.

References

References

Anderson, W. E. & Yang, V. (1995), *Liquid Rocket Engine Combustion Instability*, Vol. 169 of *Progress in Astronautics and Aeronautics*, American Institute of Aeronautics and Astronautics.

Baillot, F., Blaisot, J.-B., Boisdron, G. & Dumouchel, C. (2009), 'Behaviour of an air-assisted jet submitted to a transverse high-frequency acoustic field', *Journal of Fluid Mechanics* **640**, 305–342.

Brackbill, J. U., Kothe, D. B. & Zemach, C. (1992), 'A continuum method for modeling surface tension', *Journal of Computational Physics* **100**(2), 335–354.

Buffum, F. G. & Williams, F. A. (1967), 'Response of Turbulent Jets to Transverse Acoustic Fields', *Proceedings of the 1967 Heat Transfer and Fluid Mechanics Institute* pp. 247–276.

Chehroudi, B. & Talley, D. (2002), Interaction of acoustic waves with a cryogenic nitrogen jet at sub- and supercritical pressures, *in* '40th AIAA Aerospace Sciences Meeting & Exhibit', Reno, Nevada.

Chiapolino, A., Boivin, P. & Saurel, R. (2017), 'A simple and fast phase transition relaxation solver for compressible multicomponent two-phase flows', *Computers & Fluids* **150**, 31–45.

Crocco, L. & Zheng, X. (1956), *Theory of combustion instability in liquid propellant rocket motors*, Butterworths Scientific Publications.

Culick, F. E. C. (1976), 'Nonlinear behavior of acoustic waves in combustion chambers—I', *Acta Astronautica* **3**(9-10), 715–734.

Culick, F. E. C. (2006), *Unsteady Motions in Combustion Chambers for Propulsion Systems*, AGARDograph, NATO/RTO-AG-AVT-039.

Davis, D. W. & Chehroudi, B. (2007), 'Measurements in an Acoustically Driven Coaxial Jet under Sub-, Near-, and Supercritical Conditions', *Journal of Propulsion and Power* **23**(2), 364–374.

Downar-Zapolski, P., Bilicki, Z., Bolle, L. & Franco, J. (1996), 'The non-equilibrium relaxation model for one-dimensional flashing liquid flow', *International Journal of Multiphase Flow* **22**(3), 473–483.

Dufour, G., Massot, M. & Villedieu, P. (2003), 'Étude d'un modèle de fragmentation secondaire pour les brouillards de gouttelettes', *Comptes Rendus Mathematique* **336**(5), 447–452.

Emre, O., Kah, D., Jay, S., Tran, Q.-H., Velghe, A., de Chaisemartin, S., Fox, R. O., Laurent, F. & Massot, M. (2015), 'Eulerian moment methods for automotive sprays', *Atomization and Sprays* **25**(3), 189–254.

Ficuciello, A. (2017), Analysis of high frequency/high amplitude acoustic field effects on coaxial injection: application to liquid rocket engines, PhD thesis, Université Rouen Normandie.

Ficuciello, A., Blaisot, J.-B., Richard, C. & Baillot, F. (2017), 'Investigation of air-assisted sprays submitted to high frequency transverse acoustic fields: Droplet clustering', *Physics of Fluids* **29**(6), 067103.

Gaillard, P., Le Touze, C., Matuszewski, L. & Murrone, A. (2016), 'Numerical simulation of cryogenic injection in rocket engine combustion chambers', *AerospaceLab Journal* **11**.

Goncalvès, E. (2014), 'Modeling for non isothermal cavitation using 4-equation models', *International Journal of Heat and Mass Transfer* **76**, 247–262.

Gonzalez-Flesca, M., Schmitt, T., Ducruix, S. & Candel, S. (2016), 'Large eddy simulations of a transcritical round jet submitted to transverse acoustic modulation', *Physics of Fluids* **28**(5), 055106.

Greenberg, J. B., Silverman, I. & Tambour, Y. (1993), 'On the origins of spray sectional conservation equations', *Combustion and Flame* **93**(1-2), 90–96.

Hakim, L., Ruiz, A., Schmitt, T., Boileau, M., Staffelbach, G., Ducruix, S., Cuenot, B. & Candel, S. (2015), 'Large eddy simulations of multiple transcritical coaxial flames submitted to a high-frequency transverse acoustic modulation', *Proceedings of the Combustion Institute* **35**(2), 1461–1468.

Hakim, L., Schmitt, T., Ducruix, S. & Candel, S. (2015), 'Dynamics of a transcritical coaxial flame under a high-frequency transverse acoustic forcing: Influence of the modulation frequency on the flame response', *Combustion and Flame* **162**(10), 3482–3502.

Hardi, J. S., Martinez, H. C. G., Oschwald, M. & Dally, B. B. (2014), 'LOx Jet Atomization Under Transverse Acoustic Oscillations', *Journal of Propulsion and Power* **30**(2), 337–349.

Harrje, D. T. & Reardon, F. H. (1972), *Liquid propellant rocket combustion instability*, NASA Special Publication 194.

Herrmann, M. (2010), 'A parallel Eulerian interface tracking/Lagrangian point particle multi-scale coupling procedure', *Journal of Computational Physics* **229**(3), 745–759.

Herrmann, M. (2011), 'On simulating primary atomization using the refined level set grid method', *Atomization and Sprays* **21**(4), 283–301.

Hoover, D. V., Ryan, H. M., Pal, S., Merkle, C. L., Jacobs, H. R. & Santoro, R. J. (1991), 'Pressure Oscillation Effects on Jet Breakup', *Heat and Mass Transfer in Spray Systems* **187**, 27–36.

Jay, S., Lacas, F. & Candel, S. (2006), 'Combined surface density concepts for dense spray combustion', *Combustion and Flame* **144**(3), 558–577.

Kim, D. & Moin, P. (2011), Numerical simulation of the breakup of a round liquid jet by a coaxial flow of gas with a subgrid Lagrangian breakup model, *in* 'Center for Turbulence Research Annual Research Briefs'.

King, L. V. (1934), 'On the Acoustic Radiation Pressure on Spheres', *Proceedings of the Royal Society A: Mathematical, Physical and Engineering Sciences* **147**(861), 212–240.

Lafaurie, B., Nardone, C., Scardovelli, R., Zaleski, S. & Zanetti, G. (1994), 'Modelling Merging and Fragmentation in Multiphase Flows with SURFER', *Journal of Computational Physics* **113**(1), 134–147.

Langenais, A., Vuillot, F., Troyes, J. & Bailly, C. (2018), 'Accurate simulation of the noise generated by a hot supersonic jet including turbulence tripping and nonlinear acoustic propagation', *Physics of Fluids* **31**.

Lasheras, J. C. & Hopfinger, E. J. (2000), 'Liquid Jet Instability and Atomization in a Coaxial Gas Stream', *Annual Review of Fluid Mechanics* **32**(1), 275–308.

Laurent, F. & Massot, M. (2001), 'Multi-fluid modelling of laminar polydisperse spray flames: origin, assumptions and comparison of sectional and sampling methods', *Combustion Theory and Modelling* **5**(4), 537–572.

Le Touze, C. (2015), Couplage entre modèles diphasiques à « phases séparées » et à « phase dispersée » pour la simulation de l'atomisation primaire en combustion cryotechnique, PhD thesis, University of Nice Sophia Antipolis.

Le Touze, C., Murrone, A. & Guillard, H. (2015), 'Multislope MUSCL method for general unstructured meshes', *Journal of Computational Physics* **284**, 389–418.

Lilly, D. K. (1967), The representation of small-scale turbulence in numerical simulation experiments, *in* 'IBM Scientific Computing Symposium on Environmental Sciences', White Plains, New York.

Marmottant, P. & Villermaux, E. (2004), 'On spray formation', *Journal of Fluid Mechanics* **498**, 73–111.

Miesse, C. C. (1955), 'The Effect of Ambient Pressure Oscillations on the Disintegration and Dispersion of a Liquid Jet', *Journal of Jet Propulsion* **25**(10), 525–530.

Murrone, A., Fdida, N., Le Touze, C. & Vingert, L. (2014), Atomization of cryogenic rocket engines coaxial injectors. Modeling aspects and experimental investigations., Cologne, Germany.

Murrone, A. & Villedieu, P. (2011), 'Numerical Modeling of Dispersed Two-Phase Flows', *AerospaceLab Journal* **2**.

Méry, Y., Hakim, L., Scouflaire, P., Vingert, L., Ducruix, S. & Candel, S. (2013), 'Experimental investigation of cryogenic flame dynamics under transverse acoustic modulations', *Comptes Rendus Mécanique* **341**(1-2), 100–109.

Noiray, N., Durox, D., Schuller, T. & Candel, S. (2008), 'A unified framework for nonlinear combustion instability analysis based on the flame describing function', *Journal of Fluid Mechanics* **615**, 139.

Oefelein, J. C. & Yang, V. (1993), 'Comprehensive review of liquid-propellant combustion instabilities in F-1 engines', *Journal of Propulsion and Power* **9**(5), 657–677.

Pilch, M. & Erdman, C. (1987), 'Use of breakup time data and velocity history data to predict the maximum size of stable fragments for acceleration-induced breakup of a liquid drop', *International Journal of Multiphase Flow* **13**(6), 741–757.

Poinsot, T. (2017), 'Prediction and control of combustion instabilities in real engines', *Proceedings of the Combustion Institute* **36**(1), 1–28.

Pope, S. B. (2000), *Turbulent flows*, Cambridge University Press.

Refloch, A., Courbet, B., Murrone, A., Villedieu, P., Laurent, C., Gilbank, P., Troyes, J., Tessé, L., Chaineray, G., Dargaud, J., Quémerais, E. & Vuillot, F. (2011), 'CEDRE Software', *AerospaceLab Journal* **2**.

Rey, C., Ducruix, S. & Candel, S. (2005), 'A method for the transverse modulation of reactive flows with application to combustion instability', *Combustion Theory and Modelling* **9**(1), 5–22.

Saurel, R. & Lemetayer, O. (2001), 'A multiphase model for compressible flows with interfaces, shocks, detonation waves and cavitation', *Journal of Fluid Mechanics* **431**, 239–271.

Schiller, L. & Naumann, A. (1935), 'A drag coefficient correlation', *Zeitschrift des Vereines Deutscher Ingenieure* pp. 318–320.

Selle, L., Blouquin, R., Théron, M., Dorey, L.-H., Schmid, M. & Anderson, W. (2014), 'Prediction and Analysis of Combustion Instabilities in a Model Rocket Engine', *Journal of Propulsion and Power* **30**(4), 978–990.

Sibra, A., Dupays, J., Murrone, A., Laurent, F. & Massot, M. (2017), 'Simulation of reactive polydisperse sprays strongly coupled to unsteady flows in solid rocket motors: Efficient strategy using Eulerian Multi-Fluid methods', *Journal of Computational Physics* **339**, 210–246.

Smagorinsky, J. (1963), 'General circulation experiments with the primitive equations: I. the basic experiment*', *Monthly Weather Review* **91**(3), 99–164.

Sun, Y. & Beckermann, C. (2004), 'Diffuse interface modeling of two-phase flows based on averaging: mass and momentum equations', *Physica D* **198**(3-4), 281–308.

Urbano, A., Selle, L., Staffelbach, G., Cuenot, B., Schmitt, T., Ducruix, S. & Candel, S. (2016), 'Exploration of combustion instability triggering using Large Eddy Simulation of a multiple injector liquid rocket engine', *Combustion and Flame* **169**, 129–140.

Varoquié, B., Légier, J., Lacas, F., Veynante, D. & Poinsot, T. (2002), 'Experimental analysis and large eddy simulation to determine the response of non-premixed flames submitted to acoustic forcing', *Proceedings of the Combustion Institute* **29**(2), 1965–1970.

Villermaux, E. (1998), 'Mixing and Spray Formation in Coaxial Jets', *Journal of Propulsion and Power* **14**(5), 807–817.

Wert, K. L. (1995), 'A rationally-based correlation of mean fragment size for drop secondary breakup', *International Journal of Multiphase Flow* **21**(6), 1063–1071.

Williams, F. A. (1958), 'Spray Combustion and Atomization', *Physics of Fluids* **1**(6), 541.

Wu, J., Du, G., Work, S. S. & Warshaw, D. M. (1990), 'Acoustic radiation pressure on a rigid cylinder: An analytical theory and experiments', *The Journal of the Acoustical Society of America* **87**(2), 581.

Zhuk, A. P. (1986), 'Radiation force acting on a cylindrical particle in a sound field', *International Applied Mechanics* **22**(7), 689–693.

Zuzio, D., Estivalèzes, J.-L. & DiPierro, B. (2016), 'An improved multiscale Eulerian–Lagrangian method for simulation of atomization process', *Computers and Fluids* .

Zuzio, D., Estivalèzes, J.-L., Villedieu, P. & Blanchard, G. (2013), 'Numerical simulation of primary and secondary atomization', *Comptes Rendus Mécanique* **341**(1-2), 15–25.